Earth Planet. Sci. Lett. 643 (2024) 118888

Contents lists available at ScienceDirect

Earth and Planetary Science Letters

journal homepage: www.elsevier.com/locate/epsl

Unraveling the tectonic evolution of the Andean hinterland (Argentina and Chile, 30°S) using multi-sample thermal history models

Chelsea Mackaman-Lofland [a,c,*], Ana C. Lossada [b], Julie C. Fosdick [c], Vanesa D. Litvak [b], María Pía Rodríguez [d], Macarena Bertoa del Llano [e], Richard A. Ketcham [f], Daniel F. Stockli [f], Brian K. Horton [f,g], José Mescua [e,h], Julieta Suriano [e], Laura Giambiagi [e]

[a] Department of Earth & Environmental Sciences, Denison University, Granville, OH, USA
[b] Instituto de Estudios Andinos Don Pablo Groeber (IDEAN, University of Buenos Aires-CONICET), Buenos Aires, Argentina
[c] Department of Earth Sciences, University of Connecticut, Storrs, CT, USA
[d] Carrera de Geología, Facultad de Ingeniería, Universidad Andrés Bello, Santiago 8370134, Chile
[e] IANIGLA, CCT Mendoza, CONICET, Mendoza, Argentina
[f] Department of Earth and Planetary Sciences, Jackson School of Geosciences, University of Texas at Austin, Austin, TX, USA
[g] Institute for Geophysics, Jackson School of Geosciences, University of Texas at Austin, Austin, TX, USA
[h] Facultad de Ciencias Exactas y Naturales, Universidad Nacional de Cuyo, USA

ARTICLE INFO

Editor: Dr A Webb

Keywords:
Andes
Hinterland
Exhumation
Thermochronology
Thermal history modeling
Subduction

ABSTRACT

The Andean hinterland of Chile and Argentina defines a region of voluminous magmatism, polyphase deformation, and high topography above a long-lived subduction zone. Construction of this high-elevation domain has been variably attributed to isostatic uplift during crustal thickening induced by internal hinterland shortening, underthrusting during growth of the external thrust belt, or lower crustal flow. Alternatively, uplift may be related to dynamic processes associated with lithospheric foundering or flat-slab subduction. This study integrates geo/thermochronological, structural, magmatic, and sedimentological datasets to reconstruct hinterland evolution and evaluate potential drivers of exhumation. Our thermal history modeling approach implements a new time-depth extension to HeFTy 2 software, which enables simultaneous inversion of multiple samples along a structural or topographic profile. This extension addresses transient effects such as isotherm deflection and the transition from geothermal to atmospheric gradients and permits changes in the relative position among samples (folding, tilting) within user-defined constraints. Single- and multi-sample modeling results based on published apatite (U-Th)/He and fission track data (AHe, AFT) along the western Andean hinterland confirm late Eocene (~30–40 Ma) cooling below at least ~120°C, whereas thermal histories derived from new AHe, AFT, and zircon He analyses from the eastern hinterland resolve Mesozoic cooling below ~80–160°C, followed by protracted residence at ~60–80°C and rapid exhumational cooling in the early Miocene. Multi-sample models further require ~10° eastward tilting of eastern sample locations, compatible with hinterland uplift via underthrusting and development of a crustal-scale fault-bend fold that was geometrically and kinematically linked to shortening in the external (eastern) thrust belt. Results underscore the enhanced resolution of multi-sample thermal history models in testing structural hypotheses and deciphering the timing, magnitude, and mechanisms of exhumational cooling during changing geodynamic conditions.

1. Introduction

Cordilleran hinterland regions define high-elevation tectonic domains in orogenic interiors distinct from the zones of maximum upper-crustal shortening in the flanking external thrust belts. Various mechanisms have been proposed to control hinterland topographic growth, including internal deformation, thickening due to underthrusting, magmatic addition, lower crustal flow, and deeper processes associated with lithospheric foundering, mantle convection, and subduction dynamics (e.g., Allmendinger et al., 1990; Beck and Zandt, 2002; Carrapa et al., 2022; Giambiagi et al., 2022; Horton et al., 2022; Long, 2023; McQuarrie, 2002). Understanding the influence of these processes

* Corresponding author: Department of Earth, Environmental, & Planetary Sciences, University of Tennessee, Knoxville, TN, USA.
E-mail address: cmackama@utk.edu (C. Mackaman-Lofland).

https://doi.org/10.1016/j.epsl.2024.118888
Received 19 December 2023; Received in revised form 26 April 2024; Accepted 9 July 2024
Available online 24 July 2024

remains complicated by questions regarding the timing and nature of hinterland deformation, the role of magmatic addition, and mechanical and kinematic linkages—or the lack thereof—between hinterland crustal thickening and thrust belt structures.

At ~30°S (Fig. 1), the Andean hinterland of Chile and western Argentina defines a ~100-km-wide, high elevation (>3–6 km) domain that recorded arc- and extension-related magmatism, polyphase deformation, bedrock exhumation, volcano-sedimentary basin accumulation, and topographic uplift during subduction along the western margin of South America. Debate persists over signatures of exhumational cooling identified in the western hinterland and the role of internal shortening (Fosdick et al., 2015; 2017; Lossada et al., 2017; Mackaman-Lofland et al., 2019; Rodríguez et al., 2018), as well as the geometry and kinematics of subsurface structures that may accommodate underthrusting via linkages between hinterland and retroarc thrust belt domains (Allmendinger et al., 1990; Ammirati et al., 2022; Giambiagi et al., 2017; 2022; Mackaman-Lofland et al., 2022). Construction of this hinterland segment has been further attributed to lower crustal flow from regions of excess crustal thickness and dynamic topography during flat-slab subduction (Carrapa et al., 2022; Dávila and Lithgow-Bertelloni, 2015). Evaluating the relative influence of these processes is timely, as new mapping and geochronologic analyses have refined chronostratigraphic and structural relationships along the Chilean orogenic flank at ~30°S (Murillo et al., 2017; Velásquez et al., 2021). Advances in numerical modeling tools further enable the quantitative integration of spatial, structural, and geo/thermochronological datasets to interrogate thermotectonic hypotheses (Ketcham, 2024).

Here we integrate geochronology, low-temperature thermochronology, and structural, sedimentological, and geochemical datasets to connect construction of the Andean hinterland with deformation, magmatism, and burial/exhumation events. Our thermal history modeling approach utilizes a new time-depth extension to HeFTy 2 software that, for the first time, enables simultaneous inversion of multiple surface samples and permits shifts in their relative position (via topographic evolution or structural tilting) within user defined constraints (Ketcham, 2024). Single- and multi-sample models based on published geo/-thermochronological data confirm at least ~120°C of exhumation-driven cooling along the western Andean flank by middle to late Eocene time. New geo/thermochronological data and multi-sample inversion results from the eastern (retroarc) hinterland constrain protracted Mesozoic–Paleogene sample residence at ~60–120°C followed by up to ~60–80°C of rapid exhumational cooling and structural tilting synchronous with Neogene retroarc thrust belt advance. Our findings demonstrate the utility of multi-sample time-depth modeling in improving upon single-sample modeling approaches and highlight the role of structural processes—including minor late Eocene internal shortening and Miocene underthrusting kinematically linked to external thrust belt development—in governing thermal signatures of uplift-induced exhumation in the Andean hinterland.

2. Geologic & geodynamic context

Western South America has persisted as an ocean-continent convergent margin since late Paleozoic–early Mesozoic time (Capaldi et al., 2021; Charrier et al., 2007; Mpodozis and Ramos, 1990). At ~30°S, the Andes overlie a modern zone of flat-slab subduction and are divided into five tectonic domains: the Coastal Cordillera, Principal and Frontal Cordilleras, Precordillera, and Sierras Pampeanas (Fig. 1). The boundary between the Coastal and Principal Cordilleras defines the western Andean topographic flank. The Principal and Frontal Cordilleras comprise a ~100 km-wide hinterland region of >3–6 km elevation, former arc magmatism, and limited internal deformation. The Precordillera retroarc thrust belt accommodated the majority of shortening (>65–100 km) with unclear kinematic links between a regional,

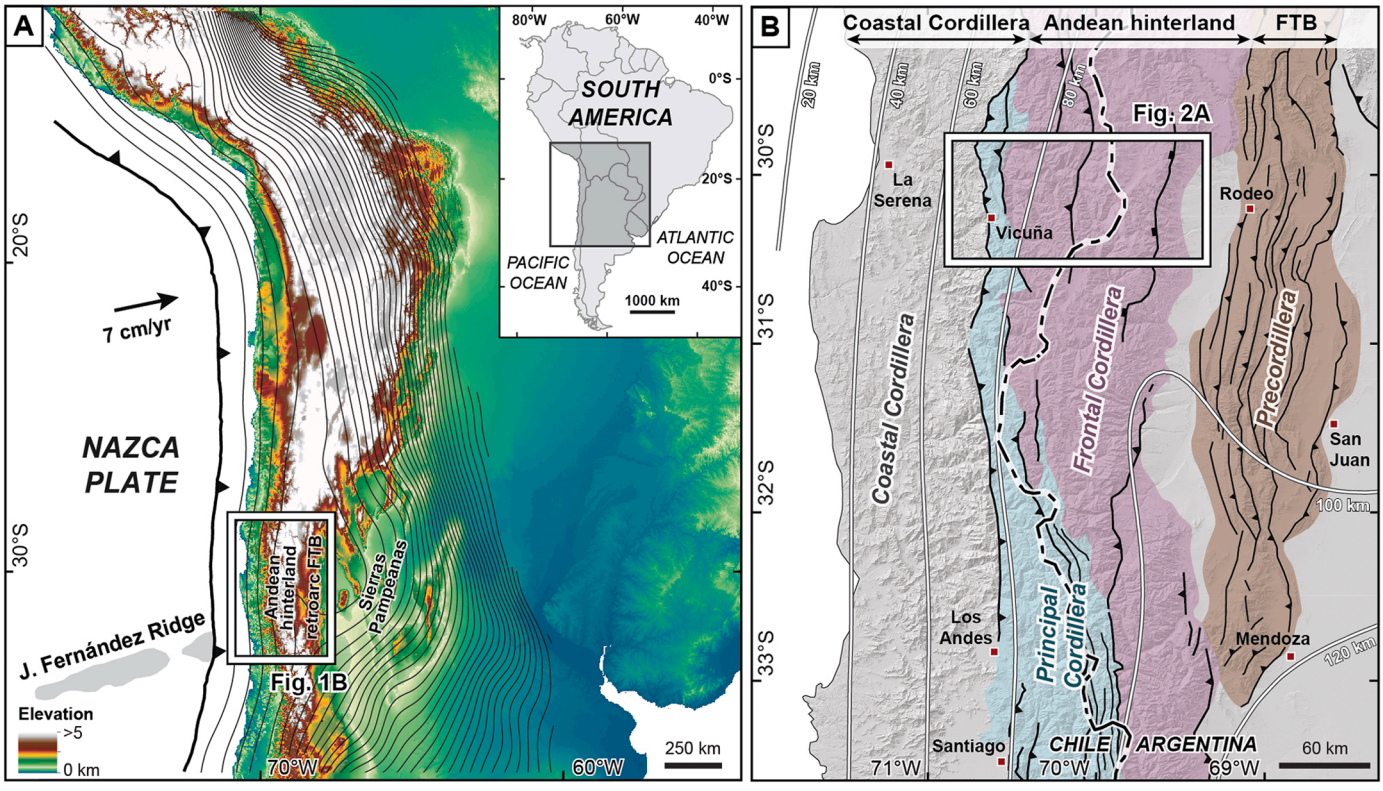

Fig. 1. (A) Map of the Central Andes showing topography (ASTER DEM V002), tectonic setting, and study location. Nazca-South America plate convergence rates from Ramos and Folguera (2009). Modern trench location (thick black line with teeth) and Wadati-Benioff zone contours (thin black lines; 40 km contour interval) after Hayes et al. (2018). FTB: fold-thrust belt. Inset map denotes location within South America. (B) Regional map illustrating major faults and Principal Cordillera, Frontal Cordilleran and Precordillera structural domains (Sierras Pampeanas located ~10–20 km east of the map area).

west-dipping décollement and deeper crustal structures beneath the Frontal or Principal Cordilleras (Allmendinger et al., 1990; Giambiagi et al., 2017; Heredia et al., 2002; Mackaman-Lofland et al., 2022). The Sierras Pampeanas comprise basement-cored uplifts that partition the distal foreland. Neogene shallowing of the subducted plate is constrained by the inboard expansion and cessation of arc magmatism and onset of basement-involved deformation in the Sierras Pampeanas (Horton et al., 2022; Ramos et al., 2002), and is generally attributed to subduction of the Juan Fernández aseismic ridge starting at ~12–10 Ma (Yáñez et al., 2001).

This study focuses on the Principal and Frontal Cordillera hinterland domains (Figs. 1, 2). Along the studied E-W profile, the Principal Cordillera is limited to a ~15-km-wide belt of Triassic–Cretaceous volcaniclastic and sedimentary strata bounded by the Vicuña and Rivadavia faults (Fig. 2). The western Frontal Cordillera comprises a ~40–60-km-wide region of Carboniferous–Triassic granitoid batholiths (including the Elqui-Limarí complex and Guanta/other subsidiary plutons) deformed by high-angle reverse faults such as the Punilla-La Plata and Baños del Toro faults (Fig. 2; Murillo et al., 2017). Along the international border, east- and west-dipping thrust and strike-slip faults of the El Indio-Valle del Cura belt deform volcanic and volcaniclastic Choiyoi Group (Permian-Triassic) and Valle del Cura (Paleogene–Neogene) basin deposits (Murillo et al., 2017). Along the retroarc hinterland slope, the eastern Frontal Cordillera exposes Permian–Triassic granitoids, voluminous Choiyoi Group synextensional deposits bounded by listric, partially inverted normal faults (e.g., Las Leñas fault; Fig. 2), and gently east-dipping Carboniferous–Permian strata atop deformed Devonian rocks (Heredia et al., 2002). Dip measurements of Carboniferous–Permian strata average ~10–12° east-southeast, and seismic reflection data from the adjacent Iglesia Basin show wedgetop strata onlapping a ~12° east-dipping bedrock surface (Allmendinger et al., 1990). Jurassic–Paleogene rocks are largely absent from this eastern region, though the Choiyoi succession is locally capped and intruded by Cenozoic sedimentary and igneous rocks (Cardó and Díaz, 2005; Heredia et al., 2002).

Published geochronological and geochemical data help constrain hinterland magmatism and deformation. At ~30°S, zircon U-Pb, Rb-Sr, K-Ar, and $^{40}Ar/^{39}Ar$ results confirm emplacement of the Elqui-Limarí granitoid plutons at ~260–330 Ma, the Choiyoi Group igneous complex at ~240–285 Ma, and generally eastward-younging, smaller-volume plutons during the Late Triassic–Neogene (Fig. 2; Table 1; Jones et al., 2016; Murillo et al., 2017; Rodríguez et al., 2018; Sato et al., 2015). Petrographic, geochemical, and isotopic analyses indicate subduction-related magmatism concurrent with Carboniferous–middle Permian crustal thickening followed by arc and backarc magmatism with geochemical signatures suggestive of crustal thinning during Permian–Triassic postorogenic collapse and backarc extension (Capaldi et al., 2021; Kleiman and Japas, 2009; Mpodozis and Ramos, 1990). Late Triassic–Neogene magmatism during protracted subduction involved: (1) juvenile arc and backarc activity during Triassic–Early Cretaceous slab rollback and neutral to extensional conditions in the overriding plate; (2) relatively evolved isotopic signatures associated with Late Cretaceous shortening; (3) scarce crustal contributions and enhanced melting of the mantle wedge during the latest Cretaceous–Eocene; (4) volcanic and hypabyssal pluton emplacement controlled by normal faulting and intra-arc extension, notably within the El Indio-Valle del Cura region, during the Oligocene–early Miocene; and (5) increased crustal assimilation and thicknesses concurrent with Miocene inversion of hinterland normal faults, Precordillera shortening, and eastward arc expansion (Capaldi et al., 2021; Giambiagi et al., 2017; Jones et al., 2016; Litvak et al., 2007; 2018). Crosscutting relationships with the above igneous units constrain the timing of motion along individual faults. The Principal and Frontal Cordilleras have been largely amagmatic above the flat-slab segment since ~9–6 Ma (Bissig et al., 2001; Litvak et al., 2018; Ramos et al., 2002).

Low-temperature thermochronology data provide insight into the thermal history of the hinterland and adjacent domains. Published apatite (U-Th)/He (AHe) and fission track (AFT) analyses from igneous rocks along the Principal and western Frontal Cordillera span ~1–4 km elevation and produced <10 to 40 Ma AHe dates, ~25–40 Ma AFT central or pooled ages with relatively long (>13–15 μm) mean track lengths, and positive age-elevation relationships that have been ascribed to late Eocene and middle Miocene phases of exhumational cooling (Fig. 2; Lossada et al., 2017; Rodríguez et al., 2018). AHe, AFT, and zircon (U-Th)/He (ZHe) data from the Colangüil batholith in the eastern hinterland yielded ~5 Ma AHe dates, ~30–36 Ma AFT ages with short (<11 μm) mean track lengths, and ~185–235 Ma ZHe dates that have been attributed to early Mesozoic cooling below ~180 °C, protracted residence in the AFT partial annealing zone, and possible late Eocene–Oligocene and/or Miocene–Pliocene exhumational cooling (Fig. 2; Fosdick et al., 2015; Lossada et al., 2017). Thermochronology data and synorogenic basin fill constrain shortening in the adjacent Precordillera thrust belt from ~16–15 to 2 Ma, with a notable increase in shortening and exhumation at ~12–9 Ma (Fosdick et al., 2015; Jordan et al., 1993; Levina et al., 2014; Mackaman-Lofland et al., 2022; Suriano et al., 2017).

Finally, in the Principal Cordillera and possibly Frontal Cordillera south of the study area, Choiyoi Group and other late Paleozoic igneous rocks were buried by up to ~2–4 km of Triassic–Neogene backarc, retroarc foreland, and intra-arc basin fill (Cristallini and Ramos, 2000; Mackaman-Lofland et al., 2019). Interpretations of late Eocene through late Oligocene distal foreland basin sedimentation based on thin (<0.4 km) deposits in the eastern Frontal Cordillera and frontal Precordillera (Fosdick et al., 2017; Suriano et al., 2023) require accumulation and rapid removal of a thicker foredeep succession across the Frontal Cordillera and Precordillera domains. Prior to this study, the extent to which Mesozoic–Cenozoic burial reheating affected the region was unknown.

3. Geo- & thermochronology analyses

3.1. Methods

We augment published data with 17 new geochronology and low-temperature thermochronology analyses, obtained from seven igneous and sedimentary samples from the eastern Frontal Cordillera. Four igneous samples comprise Choiyoi Group granodiorite from the 12 km^2 Agua Negra pluton, whereas three sedimentary samples were obtained from turbiditic sandstones of the Agua Negra Formation (Figs. 2, S1; Cardó and Díaz, 2005; Sato et al., 2015). Zircon U-Pb geochronology provides crystallization age information for igneous rocks and maximum depositional age and provenance data for sedimentary deposits. Low-temperature thermochronology generates further constraints on the timing, magnitude, and rates of rock cooling or reheating in response to magmatism, burial, exhumation, and associated isotherm advection (Ketcham, 2024; Ketcham et al., 2018; Murray et al., 2018; Reiners and Brandon, 2006). ZHe, AFT, and AHe thermochronology are based on the temperature-dependent diffusive loss of radiogenic daughter products (^4He) or fission damage trails and record mineral cooling below ~50–220°C, ~60–120°C, and ~40–110°C, respectively (Flowers et al., 2009; Gleadow and Fitzgerald, 1987; Green et al., 1989; Guenthner et al., 2013). The temperature sensitivity range reflects the influence of composition, crystal size, radiation damage, and heating/cooling rate on ^4He retentivity or fission track annealing in both minerals, and factors including parent isotope zonation and ^4He injection from other minerals may cause additional dispersion in (U-Th)/He datasets (Flowers et al., 2023a).

New zircon U-Pb data were obtained for three samples (two igneous, one detrital), AFT results were acquired for two, ZHe data for four (10 total individual grains), and all seven samples were analyzed for AHe (51 total grains; Table S1). All U-Pb and ZHe analyses, and 30 AHe grain measurements, were conducted at the UTChron Laboratory at the

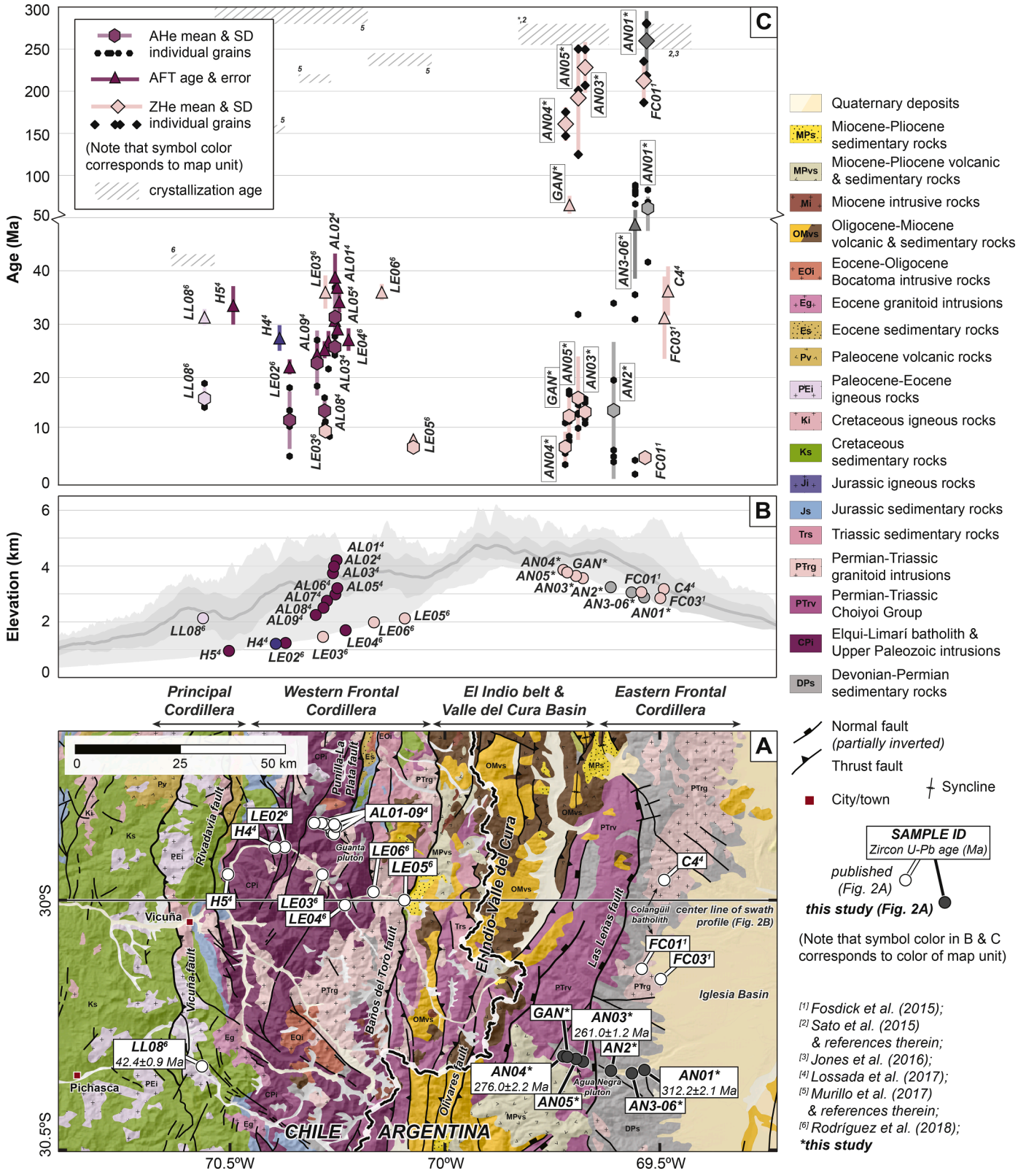

Fig. 2. (A) Geologic map with new and published thermochronology sample locations. Geochronology results obtained for the same samples are listed below sample identifiers. Geology after Cardó and Díaz (2005), Murillo et al. (2017), and Velásquez et al. (2021). (B) Topographic swath profile (80-km-wide; min/max, standard deviation, and mean elevation) and thermochronologic sample locations plotted versus distance (W-E). (C) Chart showing new and published thermochronology data and crystallization age range for host plutons.

University of Texas. All AFT measurements and 21 additional AHe grain analyses were completed at the LA.TE Andes laboratory in Salta, Argentina. Detailed analytical methods, data, and treatment parameters are reported in the Supplementary Material (Tables S2–S5).

3.2. Results & interpretations

Crystallization ages for the Agua Negra pluton were calculated from the weighted mean of the largest cluster of zircon U-Pb dates with <5% discordance and overlapping 2σ error (cluster defined using TuffZirc algorithm with outlier rejection enabled, Ludwig, 2008; Ludwig and Mundil, 2002; Fig. 3A-B). Sample AN03 yielded an age of 260.98±1.18 Ma, while AN04 produced an age of 276.03±2.21 Ma. Both results are consistent with the timing of Choiyoi Group magmatism defined by previous studies (Mackaman-Lofland et al., 2019; Sato et al., 2015).

The Agua Negra Formation detrital zircon U-Pb sample yielded a maximum depositional age (MDA) of 302.3 ± 2.1 Ma, calculated from the youngest population and equivalently, the cluster of two or more grain ages that overlap within 1σ uncertainty (n = 2 grains, Fig. 3C-D; Coutts et al., 2019; Dickinson and Gehrels, 2009). More broadly, we consider the ~300–320 Ma range of dates encompassed within the youngest age group (n = 7 grains) to approximate the time interval over which the Agua Negra sandstone resided at or near surface conditions. The data refine biostratigraphic constraints indicative of Upper Carboniferous–Lower Permian deposition of the Agua Negra Formation (Sato et al., 2015 and references therein).

New AFT, ZHe, and AHe results are plotted alongside published data to define the timing and magnitude of cooling/heating along an east-west transect spanning the Principal and Frontal Cordilleras (Fig. 2). Data for our two AFT samples (GAN, AN3–06) are shown as central ages with error reported as the relative standard deviation; radial plots are included with Table S4. Both samples pass the χ^2 test, indicative of single age populations (Galbraith, 1981; Green, 1981). Sample AN3–06, collected from the Upper Carboniferous–Lower Permian Agua Negra Formation, yielded a central AFT age of 48.7 ± 10.2 Ma, with a mean confined track length of 12.9 ± 1.3 (n = 26) and Dpar values of 1.23–2.04 μm. Sample GAN, from the Agua Negra pluton, produced a central age of 65.1 ± 10.6 Ma, a mean confined track length of 13.1 ± 1.2 (n = 66), and Dpar values of 1.56–2.50 μm.

ZHe and AHe data are shown as single grain and unweighted sample mean dates (Fig. 2). ZHe single grain dates range from ~125 to 280 Ma, with variable intrasample reproducibility and date-eU or -grain size

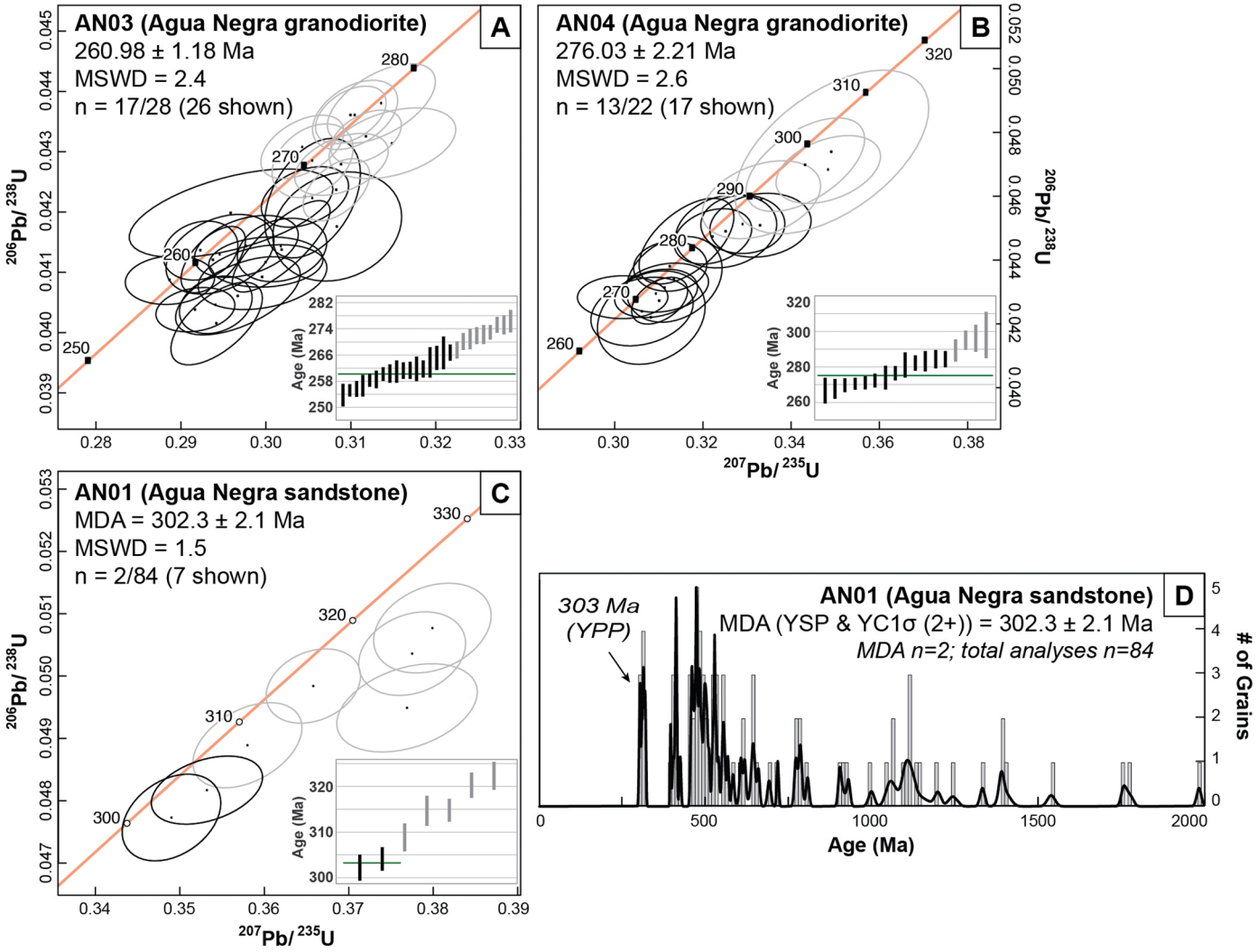

Fig. 3. Zircon U-Pb geochronology results. (A-C) Wetherill Concordia diagrams (main plots) and stack plots (insets in lower right) showing preferred crystallization ages for igneous zircon samples (A, B) and maximum depositional age for detrital sandstone sample (C). Error ellipses and bars illustrate 2σ uncertainties. Data included in each age calculation are shown in black; excluded analyses in grey. Weighted mean ages are reported with 2σ uncertainty and MSWD. (D) Age histogram and probability density plot showing detrital zircon U-Pb results. Maximum depositional age (MDA) determined from weighted mean of the youngest statistical population (YSP; equivalent to the youngest cluster of grain ages that overlap within 1σ uncertainty, YC1σ; Coutts et al., 2019; Dickinson and Gehrels, 2009).

Table 1
HeFTy 2 input table for inverse simulations of thermochronologic data (individual and multi-sample models).

1. Thermochronologic data

Samples and data used in simulations

Single-sample models

New data: AN01 (AHe & ZHe), AN2 (AHe), AN3 (AFT), AN03 (AHe & ZHe), AN04 (AHe & ZHe), AN05 (AHe & ZHe), GAN (AHe & AFT)

Published data (after Fosdick et al., 2015): FC01 (AHe & ZHe)

Published data (after Lossada et al., 2017): AL01 (AFT), AL02 (AHe & AFT), AL03 (AHe & AFT), AL05 (AFT), AL06 (AFT), AL07 (AHe & AFT), AL08 (AHe & AFT), AL09 (AHe & AFT), H4 (AFT), H5 (AFT), C4 (AFT)

Published data (after Rodríguez et al., 2018): LL08 (AHe & AFT), LE02 (AHe & AFT), LE03 (AHe, AFT), LE04 (AFT), LE05 (AHe & AFT), LE06 (AFT)

Multi-sample models

Agua Negra pluton: AN03 (AHe), AN04 (ZHe), AN05 (AHe & ZHe), GAN (AHe & AFT)

Guanta pluton: AL01 (AFT), AL02 (AHe & AFT), AL05 (AFT), AL06 (AFT), AL07 (AFT), AL08 (AHe & AFT), AL09 (AHe & AFT)

Data necessary for modeling the above samples are reported in Tables S1, S2, & S3 and the original publications; detailed HeFTy 2 inputs & modeling files are included in the Supplementary Information (Table S6)

Data treatment, uncertainties, and other relevant constraints

He data

Treatment: Unweighted mean AHe or ZHe data for each sample

He dates (Ma): Uncorrected mean dates corrected for α-ejection in HeFTy 2 (α calculation based on redistribution; stopping distances and age correction after Ketcham et al., 2011)

Error applied in modeling: Maximum of the standard deviation-based or individual uncertainty-based standard error for each sample (e.g., Flowers et al., 2023b)

Radius (μm): Unweighted mean F_T-equivalent spherical radius (Rft; after Ketcham et al., 2011)

Model precision: Good

U, Th, & Sm (ppm): Unweighted mean for each sample determined from aliquot isotope measurements and crystal morphology

AFT data

Treatment: Each sample modeled using AFT ages, c-axis projected track lengths, and D_{par} data

Initial mean track length: Determined using Dpar (μm)

Track length reduction in standard: 0.893

Kinetic populations: Determined using Dpar (μm); must pass chi-squared test (Table S2; Galbraith, 1981)

2. Additional geologic information

Constraint or hypothesis	Explanation & data source
Single-sample models	
300–320 Ma, deposition of Upper Paleozoic sandstone samples AN01, AN2, & AN3 at Earth's surface (5–25°C)	Maximum depositional age (MDA) constraint for AN01 (Fig. 3C)
590–600°C, timing dependent on crystallization age	Initial condition prior to crystallization of granitoid samples (2E; e.g., Murray et al., 2018)
260–300 Ma, 0–600°C (H5, LE02, LE04, AL01, AL02, AL03, AL05, AL06, AL07, AL08, & AL09)	Emplacement of Guanta pluton and related granites/granodiorites from zircon U-Pb, amphibole K-Ar, & amphibole $^{40}Ar/^{39}Ar$ geochronology (2Ev; Murillo et al., 2017 & references therein)
250–285 Ma, 20–600°C (FC01 & C4)	Emplacement of Colangüil granite from zircon U-Pb, whole rock Rb-Sr, & biotite Rb-Sr geochronology (2Ev; Sato et al., 2015; Jones et al., 2016)
255–280 Ma, 20–600°C (AN03, AN04, AN05, & GAN)	Emplacement of Agua Negra granodiorite from zircon U-Pb geochronology & structural/stratigraphic relationships (2Ev; Sato et al., 2015)
235–245 Ma, 20–600°C (LE05 & LE06)	Emplacement of Piuquenes monzogranite from zircon U-Pb geochronology (2Ev; Murillo et al., 2017 & references therein)
210–220 Ma, 20–600°C (LE03)	Emplacement of Los Carricitos granite from biotite & amphibole K-Ar and biotite $^{40}Ar/^{39}Ar$ geochronology (2Ev; Murillo et al., 2017 & references therein)
150–160, 0–600°C (H4)	Emplacement of Las Lechuzas diorite/granodiorite from biotite $^{40}Ar/^{39}Ar$ and zircon U-Pb geochronology (2Ev; Murillo et al., 2017)
40–45 Ma, 20–600 °C (LL08)	Emplacement of Eocene pluton from zircon U-Pb geochronology (2Ev; Rodríguez et al., 2018)
100 Ma to end of sample emplacement (~210–260 Ma), 0–600°C (all samples older than 100 Ma)	Exploratory constraint allowing for sample heating/cooling during early to middle Mesozoic magmatism, basin accumulation, and deformation events (2Ev; e.g., Cristallini and Ramos, 2000; Mackaman-Lofland et al., 2019; Murray et al., 2018)
0–100 Ma, 0–600°C (all samples older than 100 Ma)	Exploratory constraint allowing for sample heating/cooling during late Mesozoic–Cenozoic magmatism, basin accumulation, and deformation events (2Ev, maximum burial/exhumation rate 10°C/Myr; Bissig et al., 2001; Litvak et al. 2018; Lossada et al., 2017; Mackaman-Lofland et al., 2019; Suriano et al., 2023; Val et al., 2016)
0–40 Ma, 0–600°C (LL08)	Exploratory constraint allowing for sample heating/cooling during Cenozoic magmatism, basin accumulation, and deformation events (2Ev, maximum burial/exhumation rate 10°C/Myr; Bissig et al., 2001; Litvak et al., 2018; Lossada et al., 2017; Mackaman-Lofland et al., 2019; Suriano et al., 2023; Val et al., 2016)
0 Ma, present-day temperature at sample location (Table S4)	Present-day temperature determined from the modern sample elevation, mean sea level temperature (20°C), and atmospheric lapse rate (–5°C/km; Ketcham, 2024); sea level temperature and lapse rate values consistent with regional measurements and sensitivity tests (Hoke et al., 2009)
Multi-sample model: Agua Negra pluton	
Test 15, 20, 25, & 35°C/km initial geothermal gradients. Models in Fig. 6 generated using 20°C/km initial geothermal gradients, corresponding to final near-surface geothermal gradients of 25–27°C/km	Initial geothermal gradient values based on modern geothermal gradient estimates from borehole measurements, clay mineralogy, and thermochronology data (~15–35°C/km). Initial geothermal gradients of 20–25°C/km produce final near-surface geothermal gradients (~25–30°C/km) that best replicate regional data and modern geothermal estimates (e.g., Mackaman-Lofland et al., 2022 and references therein).
255–280 Ma, 29.5–30 km (corresponding to ~590–600°C using a mean sea level temperature of 20°C and initial geothermal gradient of 20°C/km)	Initial condition prior to crystallization of Agua Negra granodiorite (2E)
255–280 Ma, 1–30 km (~40–600°C using a mean sea level temperature of 20°C and initial geothermal gradient of 20°C/km)	Emplacement of Agua Negra granodiorite from zircon U-Pb geochronology & structural/stratigraphic relationships (2Ev; Sato et al., 2015)

(*continued on next page*)

Table 1 (*continued*)

100–255 Ma, 0–30 km (~0–600°C using a mean sea level temperature of 20°C and initial geothermal gradient of 20°C/km)	Exploratory constraint allowing for sample heating/cooling during early to middle Mesozoic magmatism, basin accumulation, and deformation events (2Ev; e.g., Cristallini and Ramos, 2000; Mackaman-Lofland et al., 2019; Murray et al., 2018)
0–100 Ma, 0–10 km (~0–200°C using a mean sea level temperature of 20°C and initial geothermal gradient of 20°C/km)	Exploratory constraint allowing for sample heating/cooling during late Mesozoic–Cenozoic magmatism, basin accumulation, and deformation events. Constraint also allows for the onset of topographic growth and tilting of sample positions following Late Cretaceous onset of Andean deformation (2Ev; maximum burial/exhumation rate 0.5 mm/yr; Allmendinger et al., 1990; Bissig et al., 2001; Jordan et al., 1993; Litvak et al., 2018; Lossada et al., 2017; Mackaman-Lofland et al., 2019; Mpodozis and Ramos, 1990; Suriano et al., 2023; Val et al., 2016)
0 Ma, present-day temperature at sample location (Table S4)	Present-day temperature determined from the modern sample elevation, mean sea level temperature (20°C), and atmospheric lapse rate (–5°C/km; Ketcham, 2024); sea level temperature and lapse rate values consistent with regional measurements (Hoke et al., 2009)
Multi-sample model: Guanta pluton	
Test 15, 20, 25, & 35°C/km initial geothermal gradients. Models in Fig. 6 generated using 20°C/km initial geothermal gradients, corresponding to final near-surface geothermal gradients of 25–27°C/km	Initial geothermal gradient values based on modern geothermal gradient estimates from borehole measurements, clay mineralogy, and thermochronology data (~15–35°C/km). Initial geothermal gradients of 20–25°C/km produce final near-surface geothermal gradients (~25–30°C/km) that best replicate regional data and modern geothermal estimates (e.g., Mackaman-Lofland et al., 2022 and references therein).
260–300 Ma, 29.5–30 km (corresponding to ~590–600°C using a mean sea level temperature of 20°C and initial geothermal gradient of 20°C/km)	Initial condition prior to crystallization of Guanta pluton (2E)
260–300 Ma, 1–30 km (~40–600°C using a mean sea level temperature of 20°C and initial geothermal gradient of 20°C/km)	Emplacement of Guanta pluton and related granites/granodiorites from zircon U-Pb, amphibole K-Ar, & amphibole $^{40}Ar/^{39}Ar$ geochronology (2Ev; Murillo et al., 2017 & references therein)
100–260 Ma, 0–30 km (~0–600°C using a mean sea level temperature of 20°C and initial geothermal gradient of 20°C/km)	Exploratory constraint allowing for sample heating/cooling during early to middle Mesozoic magmatism, basin accumulation, and deformation events (2Ev; e.g., Cristallini and Ramos, 2000; Mackaman-Lofland et al., 2019; Murray et al., 2018)
0–100 Ma, 0–10 km (~0–200°C using a mean sea level temperature of 20°C and initial geothermal gradient of 20°C/km)	Exploratory constraint allowing for sample heating/cooling during late Mesozoic–Cenozoic magmatism, basin accumulation, and deformation events. Constraint also allows for the onset of topographic growth following Late Cretaceous onset of Andean deformation (2Ev; maximum burial/exhumation rate 0.5 mm/yr; Allmendinger et al., 1990; Bissig et al., 2001; Jordan et al., 1993; Litvak et al., 2018; Lossada et al., 2017; Mackaman-Lofland et al., 2019; Mpodozis and Ramos, 1990; Suriano et al., 2023; Val et al., 2016)
0 Ma, present-day temperature at sample location (Table S4)	Present-day temperature determined from the modern sample elevation, mean sea level temperature (20°C), and atmospheric lapse rate (–5°C/km; Ketcham, 2024); sea level temperature and lapse rate values consistent with regional measurements (Hoke et al., 2009)
3. System- & model-specific parameters	
Kinetic models: RDAAM (Flowers et al., 2009) for AHe data; ZRDAAM (Guenthner et al., 2013) for ZHe data	
AFT annealing model: Ketcham et al. (2007)	
AFT c-axis projection: Ketcham et al. (2007), 5.5 M or 5.0 M as indicated in original publication	
Path search method: Monte Carlo	
Statistical fitting criteria: "Good" thermal histories are defined as those for which the combined probability of goodness-of-fit statistics for all input data is ≥0.5. "Acceptable" histories yield a mean goodness-of-fit value ≥0.05 (Ketcham, 2005; 2024)	
Modeling code: HeFTy v2.1.5 (Ketcham, 2024)	
End condition: 50 good paths. If good paths were not achieved after 1,000,000 paths attempted, the model end condition was modified to 1,000,000 paths attempted.	
Path segment characteristics: Listed above for each constraint. 2E (halve path segment x2; episodic randomization, monotonic-consistent cooling/heating), 2Ev (halve path segment x2; episodic randomization, monotonic-variable cooling/heating) after Ketcham (2005; 2024)	

relationships (Fig. 2; Table S5). All ZHe grain dates are younger than zircon U-Pb ages for the same samples, consistent with He loss following igneous crystallization and protracted post-emplacement cooling and/or reheating, resulting in partial to full resetting of the ZHe thermochronometer. AHe analyses range from ~2 to 90 Ma, and—with the exception of Agua Negra Formation sandstone sample AN3–06—yield single grain dates that are normally distributed and systematically younger than AFT, ZHe, and zircon U-Pb dates for the same samples or lithologies. ZHe date dispersion does not appear to correlate with lithology, but AHe dates are significantly more dispersed for two of this study's sedimentary samples (AN2 and AN3–06). Sample AN3–06 exhibited particularly poor intrasample reproducibility, including a cluster of AHe grain dates older than the AFT central age for the same sample (Fig. 2, AN3–06 reported without central tendency statistic; Flowers et al., 2023b). The AN3–06 AHe date dispersion cannot be explained by known variations in ^{4}He diffusion kinetics due to grain size or composition (Flowers et al., 2009; Reiners and Farley, 2001), and may reflect ^{4}He injection from other minerals, parent isotope zonation, and/or variations in ^{4}He inheritance from the pre-depositional thermal history of measured grains. As we are not able to constrain these possible factors, and given incompatibility with the AFT dataset, we omit the AN3–06 AHe data from further consideration.

4. Thermal history modeling (HeFTy 2)

We use inverse thermal modeling (HeFTy 2.1.7 software), coupled with geological constraints, to decipher the time-temperature/depth histories of thermochronology results and quantify the timing and magnitude of heating/cooling due to magmatism, deformation, and/or sedimentation. HeFTy inverse models quantify the thermal histories permitted by thermochronology data by generating potential time-temperature/depth paths, using kinetic equations that describe how thermochronometers respond as a function of time and temperature to predict cooling ages and, where applicable, track length distributions based on geologic and sample parameters (including crystallization/depositional age, grain size, and parent isotope concentrations), and evaluating the goodness-of-fit (GOF) between measured and modeled thermochronologic results to return thermal histories that are *supported* or *not ruled out* by the data ("good" paths with combined GOF≥0.5 and "acceptable" paths ≥0.05, respectively; Ketcham, 2005; 2024). A GOF of 0.5 represents the limit of statistical resolution; while a "best-fit" path (highest combined GOF) may be visualized to highlight an example thermal history or compare the thermal evolution of samples in a multi-sample model, it has no greater statistical or geological significance (Ketcham, 2024).

Geologic constraints for each model define the time and temperature/depth conditions of sample emplacement and present-day surface conditions derived from sample elevation and atmospheric lapse rate (–5°C/km; Hoke et al., 2009). We also include two broad constraints to permit model exploration of a variety of thermal histories and allow the data to resolve the timing and magnitude of Mesozoic–Cenozoic heating/cooling. All inverse modeling inputs are summarized in Table 1 (after Flowers et al., 2015) and the Supplementary Material (Table S6).

4.1. Single-sample inverse modeling

Single-sample inverse models yield thermal histories constrained by sample emplacement parameters, present-day surface conditions, and thermochronology data but are otherwise independent of geologic context (e.g., Fig. 4A). We present single-sample inversions for all seven new and 18 published samples from the Principal and Frontal Cordilleras, incorporating all available ZHe, AFT, and AHe data (Figs. 5, S4–S5; Fosdick et al., 2015; Lossada et al., 2017; Rodríguez et al., 2018). Two published samples (LE03, H4) yielded no "good" thermal histories after 10^6 paths were tested, and these models were omitted from further consideration. All other simulations were run until 50 "good" paths were achieved. We refer to the distribution of these "good" paths in the following summary of model results.

HeFTy simulations without ZHe constraints provide limited insight into the timing and magnitude of heating/cooling during the late Paleozoic to Paleogene: constraint-box-filling sets of paths (temperatures <20°C to 600°C) from ~250 to 40 Ma indicate the data do not inform thermal histories over this interval (e.g., AN2, AN3–06, GAN, and most published samples). In contrast, single-sample models that include ZHe data (AN01, AN03, AN04, AN05, and FC01) show a convergence of paths below ~200°C by ~200–150 Ma, reflecting the resolving power of ZHe data to rule out higher-temperature thermal histories (Figs. 5, S2). Effects of AFT and AHe data for samples from the Principal Cordillera and western Frontal Cordillera are seen in the constriction of paths below ~80–120°C by ~40–30 Ma (Fig. S3). These data resolve continued cooling at nearly constant, moderate rates (~2.5–3°C/Myr) for most lower-elevation samples (LE04, LE06, LL08, H5, AL07, AL09), whereas higher samples experienced rapid cooling (~10°C/Myr) followed by residence at or near surface temperatures (<20–40°C) from ~30 to 0 Ma (AL01–AL06; Figs. 2, S3). Thermal histories for selected western samples (LE02, LE05) reveal rapid cooling below the ~80–120°C AFT and AHe temperature sensitivity thresholds

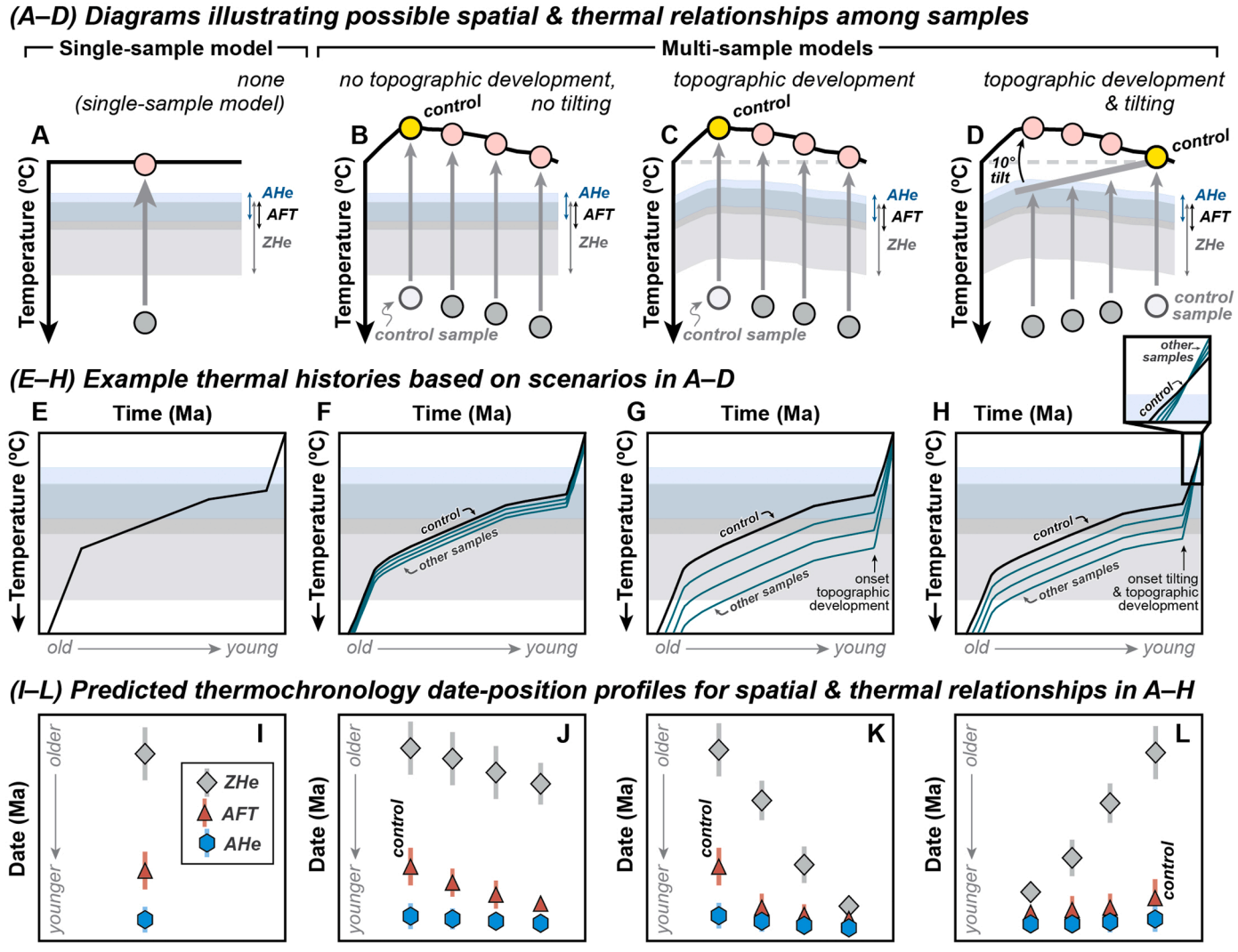

Fig. 4. (A-L) Plots showing the influence of spatial, topographic, and structural (tilting) relationships on thermochronology data. Example relationships among samples include none (single-sample model; A, E, I), spatial with no tilting or topographic development (B, F, J), spatial with full topographic development (C, G, K), and spatial with full topographic development and structural tilting (D, H, L). For each scenario, block diagrams in the top plots (A-D) illustrate spatial and thermal relationships among samples, middle plots (E-H) show example thermal histories based on the scenarios in A-D, and bottom plots (I-L) show predicted date-position patterns for synthetic thermochronology data. Note reversal of the depth relationships among samples after the onset of tilting in H.

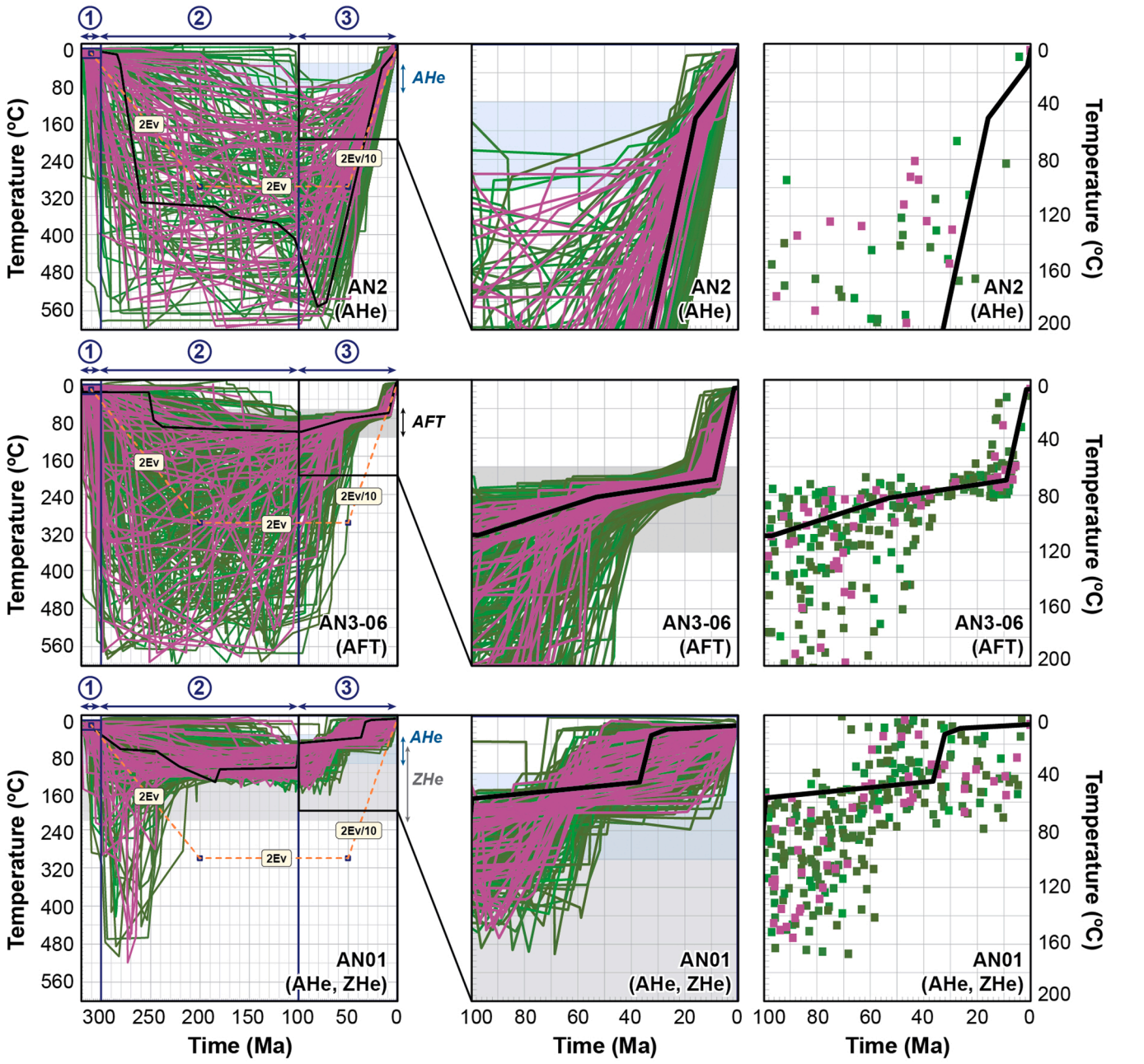

Fig. 5. Charts showing single-sample inverse thermal history models of apatite and zircon (U-Th)/He (AHe, ZHe) and apatite fission track (AFT) data obtained from Upper Paleozoic sandstones. Green, pink, and black lines denote "acceptable," "good," and best-fit time-temperature paths, respectively. Plots in the left column display thermal histories from 0 to 320 Ma alongside geologic or exploratory constraints (blue boxes), path segment characteristics (orange lines, 2Ev and 2Ev/10), and nominal partial retention/annealing zones for the AHe, AFT, and ZHe systems (based on the data included in the model; Tables 1, S6). Middle and right columns highlight time-temperature paths and HeFTy constraint points for same samples over 0–100 Ma time interval.

during the Miocene (~20 and 10 Ma, respectively; Fig. S3). AFT and AHe data in single-sample models from the eastern (retroarc) Frontal Cordillera constrain cooling below ~80°C as early as ~80–60 Ma, followed by relatively rapid final cooling starting at ~20–10 Ma (AN2, AN3–06, GAN, AN01–05, FC01, C4; Figs. 5, S2–S3).

4.2. *Multi-sample inverse modeling*

Multi-sample simulations were conducted using a time-depth extension implemented in HeFTy 2, which uses a 1-D thermal model to convert time-depth histories to time-temperature paths for evaluation

against thermochronology data. The thermal model provides a quantitative means of evolving temperature relationships in response to isotherm deflection and the transition from geothermal to atmospheric gradients, and for the first time, allows thermal histories of multiple surface samples to be modeled simultaneously (Ketcham, 2024). Multi-sample inversions can significantly improve the extent to which the solution is bounded relative to single-sample models, as time-temperature/depth paths permitted by one sample may be ruled out by another (Ketcham et al., 2018). Moreover, because the relative timing and rate of each sample's approach to the surface depends on the evolution of topography and relative sample positions (e.g., changes due to tilting/folding, Fig. 4B-D; Ketcham, 2024), the time-depth extension enables exploration of structural and spatial hypotheses such as the time-temperature/depth conditions of structural tilting or onset of topographic development.

Our multi-sample models incorporate five samples and 7 of the 11 total thermochronology datapoints from a vertical profile of the Guanta pluton, and all four samples and 6 out of 8 datapoints from the Agua Negra pluton (Table 1). We targeted these plutons because each sample group experienced simultaneous emplacement and closely related later thermal histories due to magmatic, deformation, and/or sedimentation events, as required for HeFTy 2′s multi-sample functionalities (Ketcham, 2024). We test thermal models that produce initial geothermal gradients of 15–35°C/km, corresponding to final upper-crustal geothermal gradients of ~20–40°C/km (Tables 1, S6; Figs. S4–S15). While model solutions use an initial geothermal gradient of 20°C/km (resulting in final near-surface geothermal gradients of ~25–27°C/km; Fig. 6), interpretations of burial/exhumation magnitude incorporate the range of "good"-fit thermal histories for all basal heat flux and geothermal gradient tests. Geologic and exploratory constraints were defined to achieve temperatures consistent with those accommodating magmatic heating/emplacement in single-sample models, thus, the depths in our multi-sample models are not representative of physical sample positions until the latest stages of cooling (temperatures <220°C or depths <10 km). Importantly, in our multi-sample models the 0–100 Ma exploration constraint not only allows for heating/cooling, but also defines inversion solutions for the onset of topographic development and (where applicable) structural tilting (Tables 1, S6).

Initial simulations incorporated topographic development with no structural tilting of the sample profiles (Fig. 4C). This approach yielded 50 "good" time-depth/temperature paths for the Guanta vertical profile (Figs. 6A; S5–S7), but only "acceptable" thermal histories for the Agua Negra pluton after 10^6 paths were tested, with a maximum combined GOF across all thermochronometers of 0.42 (Figs. S8–S11). We thus modified the Agua Negra model to examine the effects of ~10° eastward tilting, consistent with structural measurements and previous kinematic interpretations of eastern Frontal Cordillera construction along the forelimb of a crustal-scale fault-bend fold linked to shortening in the external (retroarc) thrust belt (Fig. 4D; Allmendinger et al., 1990; Giambiagi et al., 2017; Mackaman-Lofland et al., 2022). This inversion produced 50 "good" paths with a maximum combined GOF of 0.77 and represents our preferred solution for the Agua Negra samples (Figs. 6B, S12–S15). We refer to the distribution of "good" time-temperature paths in the following description of model results.

The AFT, AHe, and spatial data included in the Guanta simulation have limited resolving power over the late Paleozoic to Paleogene thermal history but provide excellent constraints over the past ~40 Myr (Fig. 6A; note transition from constraint-box-filling paths to tightly resolved thermal histories below AFT and AHe temperature sensitivity windows at ~40 Ma). The data reveal a two-phase history involving ~100°C of rapid, simultaneous cooling of all Guanta samples at ~40–30 Ma, followed by slower cooling at spatially variable rates from ~30 to 0 Ma (<1–1.3°C/Myr for higher-elevation samples AL01–AL02, and up to ~3°C/Myr for lowermost sample AL09). The spatial relationships among samples, combined with thermochronological data, require initiation of the early (~40–30 Ma) cooling episode at temperatures of at least ~120°C for the uppermost "control" sample (AL01) and at least ~160–200°C for lower-elevation samples AL06–AL09 (Figs. 2, 6A; note that spatial and thermochronological data do not preserve information above these temperatures and hotter path segments remain unconstrained). "Good"-fit solutions suggest the onset of cooling and inferred topographic growth by at least ~40 Ma (Fig. 6A).

Spatial, structural, and thermochronological constraints for the Agua Negra pluton provide high-resolution bounds on long-term thermal evolution (Fig. 6B). While the data permit various heating/cooling pathways until the Late Cretaceous, ZHe data (incorporated for AN04 and AN05) require residence of all samples below ~160 °C by ~170 Ma. AFT age and track length parameters (obtained for GAN) constrain slow (<0.5°C/Myr), monotonic cooling of the entire sample group below ~60–90°C from ~80 to ~15 Ma (Fig. 6B). AFT and AHe data lastly require ~60–80°C of relatively rapid cooling from ~15–5 to present. "Good"-fit inversion solutions permit the onset of east-down tilting and topographic growth over a broad time interval (~5–100 Ma), as indicated by the distribution of HeFTy constraint points in Fig. 6B. However, we emphasize that our model framework tests the hypothesis that ~10° eastward tilting occurred via hinterland translation linked to external (retroarc) shortening, and independent structural, thermochronological, and provenance datasets robustly constrain the onset of thrust belt deformation after ~16–15 Ma (Fosdick et al., 2015; Jordan et al., 1993; Levina et al., 2014; Mackaman-Lofland et al., 2022; Suriano et al., 2017).

5. Discussion

5.1. Advances in multi-sample time-depth modeling

Our results demonstrate the capability of multi-sample time-depth simulations to test spatial or structural hypotheses and improve thermal history solutions relative to single-sample models. Fig. 4 illustrates how topographic development and structural tilting may affect the thermal histories and thermochronological ages of four samples along an elevation transect (after Ketcham, 2024). In each example, a "control" sample (Ketcham, 2024) experiences early cooling below the ZHe temperature sensitivity threshold, protracted residence within the AFT partial annealing zone, and rapid late-stage cooling through the AHe partial retention zone (black paths in Fig. 4E-H; modeled after inverse solutions for the eastern Frontal Cordillera; Fig. 6B). The uplift and thermal histories of the other samples (teal paths in Fig. 4F-H) are based on their evolving relationship to the "control" sample and overlying topography (Ketcham, 2024).

Exhumational cooling with no topographic development or tilting yields parallel cooling paths wherein the only difference in thermal conditions is defined by the surface boundary above each sample (Fig. 4B, F), producing ZHe, AFT, and AHe ages that are older with increasing elevation (e.g., from right to left on block diagram and date-position plots; Fig. 4B, J). Models that incorporate full topographic development start as a peneplain, with initial temperature differences defined by the geothermal gradient. As samples exhume and topography develops, their thermal histories converge due to isotherm compression and ultimately reflect temperature differences based on the atmospheric lapse rate (Fig. 4D, H), resulting in steeper predicted age patterns (Fig. 4K). Adding 10° eastward tilting reverses the initial depth relationships among samples (Fig. 4D, H), inverting the age-position relationships for all chronometers (Fig. 4L).

Our multi-sample models for the Guanta and Agua Negra plutons leverage such patterns in the thermochronology data to explore structural and topographic hypotheses. "Good" solutions for the Guanta simulation—which incorporated samples spanning ~2–4 km elevations and permitted the onset of topographic development between 100 and 0 Ma (Figs. 4C, G)—support the hypothesis that the variations in cooling rates required for lower- versus higher-elevation samples may be explained by closely related depth/elevation-dependent thermal

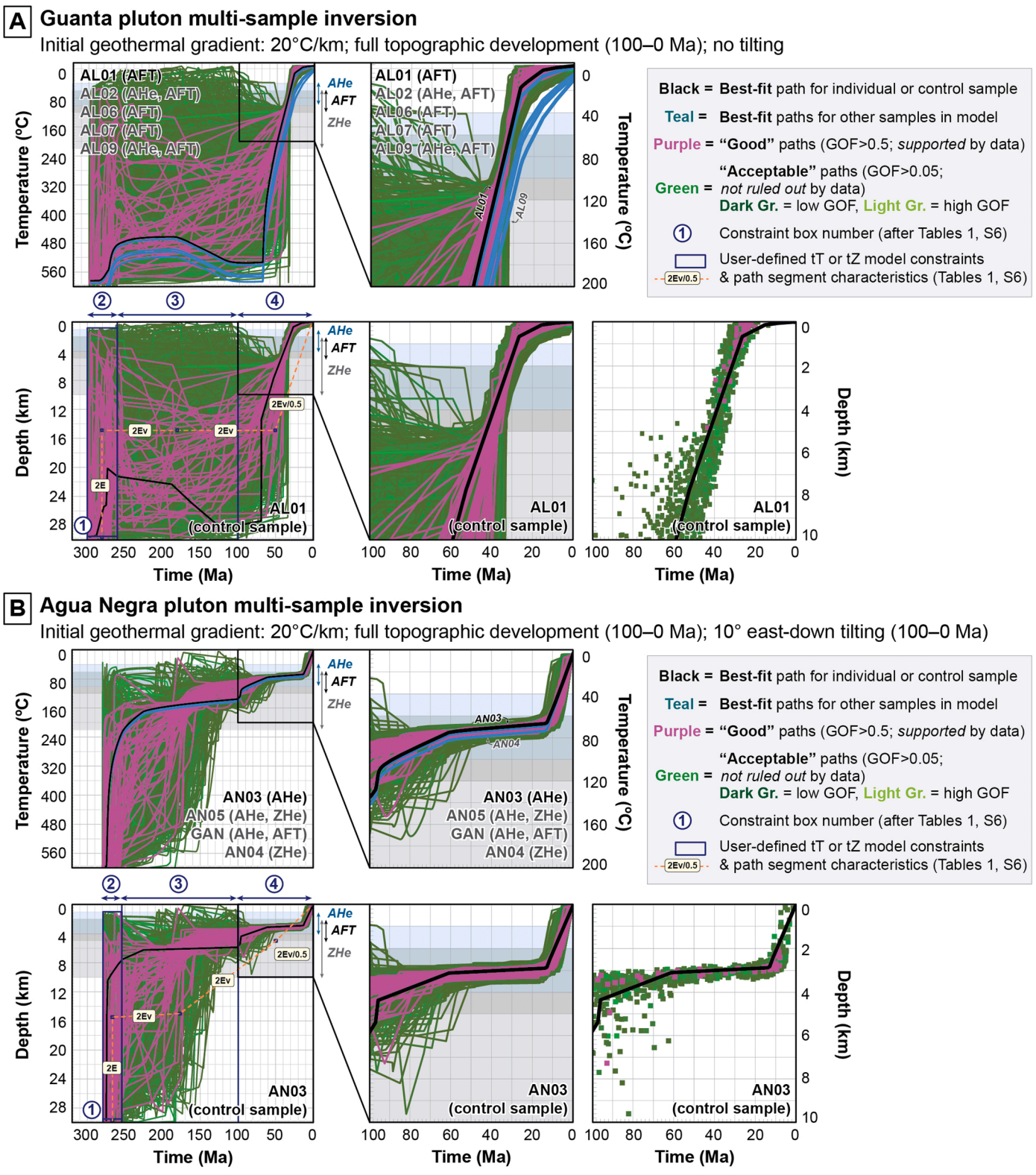

Fig. 6. Time-depth and -temperature charts showing multi-sample HeFTy inversions of apatite and zircon (U-Th)/He (AHe, ZHe) and apatite fission track (AFT) data from the Guanta (A) and Agua Negra (B) plutons. Time-depth plots also show user-defined constraints (blue boxes), path segment characteristics (orange lines; 2E, 2Ev, 2Ev/0.5), and nominal partial retention/annealing zones for the AHe, AFT, and ZHe systems given a surface temperature of 20°C and 20°C/km initial geothermal gradient (Tables 1, S6). Green, pink, and black lines denote "acceptable," "good," and best-fit paths, respectively, for the "control" sample in the multi-sample models (AL01 for the Guanta pluton, AN03 for the Agua Negra pluton). Teal lines show best-fit time-temperature paths for the other samples in the model. Left column displays thermal histories from 0 to 320 Ma; middle and right columns highlight time-temperature paths and HeFTy constraint points at 0–100 Ma. Note that constraint points <100 Ma define onset of topographic development (Guanta and Agua Negra plutons) and 10° east-down tilting (Agua Negra pluton).

histories involving rapid cooling of all samples from ~40 to 30 Ma, followed by residence of high-elevation samples near the surface and coeval cooling of lower-elevation samples during erosion and development of topographic relief (Figs. 2, 6A, S3–S7). The Agua Negra model results likewise confirm that the thermochronology data support exhumational cooling caused by topographic development and 10° east-down tilting along the eastern Frontal Cordillera (Figs. 4D, H, 6B, S12–S15). This structural setting is most compatible with hinterland construction governed by underthrusting and fault-bend fold development kinematically linked to Precordillera shortening at ~16–2 Ma (Fosdick et al., 2015; Mackaman-Lofland et al., 2022; Suriano et al., 2017). Both scenarios emphasize the importance of carefully determining and respecting the geological framework of spatial/structural hypotheses during model design and interpretation.

Finally, both Guanta and Agua Negra multi-sample simulations improve the extent to which solutions are bounded relative to single-sample models. This outcome is highlighted by a comparison of "good" paths produced by single- vs. multi-sample inversions from the Agua Negra pluton (Fig. 7). Thermal histories for the GAN single-sample model—which included AHe and AFT data—are unconstrained by the data from late Paleozoic–early Mesozoic pluton emplacement to ~80 Ma but converge within the AFT partial annealing zone from ~80 to ~15–5 Ma. In the multi-sample inversion, inclusion of ZHe data from nearby samples considerably refines the distribution of permissible late Paleozoic to Paleogene paths, requiring residence of GAN and other samples within the ZHe partial retention zone by at least ~170 Ma (Fig. 7). In turn, GAN AFT age and track length data provide important bounds on late Mesozoic–Cenozoic temperature conditions for the other samples, as shown by the narrowing of multi-sample time-temperature paths to coincide with those allowed by the GAN model from ~80 to ~15–5 Ma (Fig. 7). Final rapid cooling from ~15–5 Ma to present in the multi-sample inversion is well-constrained by GAN AFT information and AHe data from multiple samples and falls within the "good" thermal history envelopes produced by single-sample models (Figs. 7, S2).

5.2. *Mesozoic-Cenozoic thermotectonic evolution of the Andean hinterland (~30°S)*

We evaluate single- and multi-sample thermal history modeling results alongside regional geological, geochemical, and geochronological datasets to determine the influence of magmatic, deformational, and erosional events during construction of the Principal and Frontal Cordilleras. Though new and compiled thermochronology samples are consistently >5–15 km from the nearest mapped exposures of Cenozoic volcanic or intrusive rocks (Fig. 8A), we carefully consider the role of igneous activity in shaping the thermal histories of the Principal and Frontal Cordilleras, which were the locus of arc magmatism from Paleocene to middle Miocene time (Jones et al., 2016; Litvak et al., 2018). Changes in base level or climate may further modulate exhumational cooling; however, the strong correspondence between thermochronology data, modeling results, and well-documented structural and magmatic records suggests that they exerted relatively minor influence within the tectonically active Andean hinterland.

Structural, sedimentological, and provenance datasets from the Principal Cordillera and western Frontal Cordillera reveal episodes of Late Triassic to Early Cretaceous backarc extension and post-extensional thermal subsidence, followed by Late Cretaceous shortening and Paleocene volcanism during neutral tectonic conditions (Charrier et al., 2007; Litvak et al., 2018; Mackaman-Lofland et al., 2019; Mpodozis and Ramos, 1990). These events produced a >5–10 km thick basin succession in the Coastal and Principal Cordilleras, and coeval ~1–2 km thick volcanosedimentary packages preserved in the Frontal Cordillera west of the Olivares fault (Figs. 8A, 9A; Emparán and Pineda, 1999; Murillo et al., 2017; Velásquez et al., 2021). Associated burial or magmatic reheating is not recorded in our HeFTy simulations from the western hinterland (Fig. 8B-D), but models incorporating ZHe data from the eastern (retroarc) hinterland require sample residence at ~80–160°C from Middle Jurassic to Late Cretaceous time (Fig. 8E-G). Given the range of regionally permissible geothermal gradients (~15–35°C/km; Mackaman-Lofland et al., 2022 and references therein) and thickness/distribution of preserved strata, we interpret these results to reflect a ~2–4 km maximum total overburden in the eastern Frontal Cordillera during Mesozoic-early Cenozoic time (Figs. 8E-F, 9A-C, S12–S15).

The first event recorded in our thermal history models is the ~40 Ma onset of cooling in the former magmatic arc region of the western hinterland (Fig. 8B-C). Though we cannot rule out magmatic thermal effects given the unknown geometry of late Eocene–Oligocene plutons at depth, dates from fault gouge and syntectonic intrusions support reverse displacement along the Vicuña and Rivadavia faults at ~40.3–40.9 Ma (Figs. 8A, 9B; Emparán and Pineda, 1999). The Los Cuartitos Formation, a ~150 m thick package of sandstone and conglomerate deposits, further yielded ~35–41 Ma zircon U-Pb maximum depositional ages with detrital components indicative of shortening-induced exhumation along the Punilla-La Plata and Vegas Negras faults (Figs. 8A-C, 9B; Murillo et al., 2017; Velásquez et al., 2021). We thus interpret our Guanta multi-sample inversion to record rapid, shortening-induced exhumational cooling along the hanging-wall of the Punilla-La Plata fault at ~30–40 Ma, followed by slower cooling during protracted erosion and the development of topographic relief (Fig. 9F). The Guanta model does not require tilting of sample positions during cooling, consistent with relatively low-magnitude exhumation along a deeply rooted, listric structure (Fig. 9B). We interpret the minimum amount of exhumational cooling permitted by HeFTy inversions (~120°C cooling or <3–6 km of shortening-induced exhumation; Figs. 8B; S5–S7), because (1) rare earth element (REE) signatures for regional ~30–40 Ma hypabyssal intrusions indicate magma equilibration within a normal (~30–35 km) thickness crust (Fig. 8A; Bissig et al., 2001; Jones et al., 2016; Litvak et al., 2018) and (2) our best-constrained thermal history models from the eastern (retroarc) hinterland permit very little burial reheating as would be expected in response to high-magnitude shortening, flexural loading, and foreland sedimentation (Fig. 8E-G).

An Oligocene–early Miocene (~27–17 Ma) shift to hinterland extension is well constrained by geochemistry data and structural relationships within the Doña Ana and Valle del Cura basins, while crosscutting relationships confirm basin inversion accommodated by shortening along the Baños del Toro, Olivares, San Francisco, Las Leñas, and smaller faults from ~17 to 14 Ma (Fig. 9C-D; Giambiagi et al., 2017; Murillo et al., 2017; Velásquez et al., 2021; Winocur et al., 2015). These events are not clearly expressed in the thermal history models, which record slow cooling during erosion and topographic relief development west of the Punilla-La Plata fault and protracted residence at relatively low (~60–80°C) temperatures in the eastern (retroarc) hinterland (Figs. 8B-G, 9F). In this context, it is difficult to explain the ~20–15 Ma rapid cooling documented for sample LE02 (Fig. 8D). While we cannot rule out magmatic heating/cooling, most early Miocene plutons are exposed in a defined belt ~40 km to the east, and we speculate the LE02 results may record as-yet-undocumented structural exhumation along a nearby fault (Rodríguez et al., 2018).

Final rapid cooling in the eastern Frontal Cordillera coincided with high-magnitude shortening in the Precordillera starting at ~16–15 Ma (Figs. 8E-G; Jordan et al., 1993; Mackaman-Lofland et al., 2022; Suriano et al., 2017), as well as a ~16–11 Ma shift in hinterland magmatism indicative of interaction with a thickened crust (Jones et al., 2016; Litvak et al., 2007; 2018). Our multi-sample HeFTy inversion for the eastern hinterland requires both topographic development and ~10° eastward tilting. While the model itself does not constrain the timing of these events, we propose they are related to this final cooling interval, a structural scenario that accords with crustal thickening and hinterland construction via underthrusting of South American lithosphere during Precordillera shortening (Figs. 6B, 8E). In this interpretation, retroarc hinterland exhumation occurred during uplift above a major footwall ramp, followed by eastward translation along a regional décollement

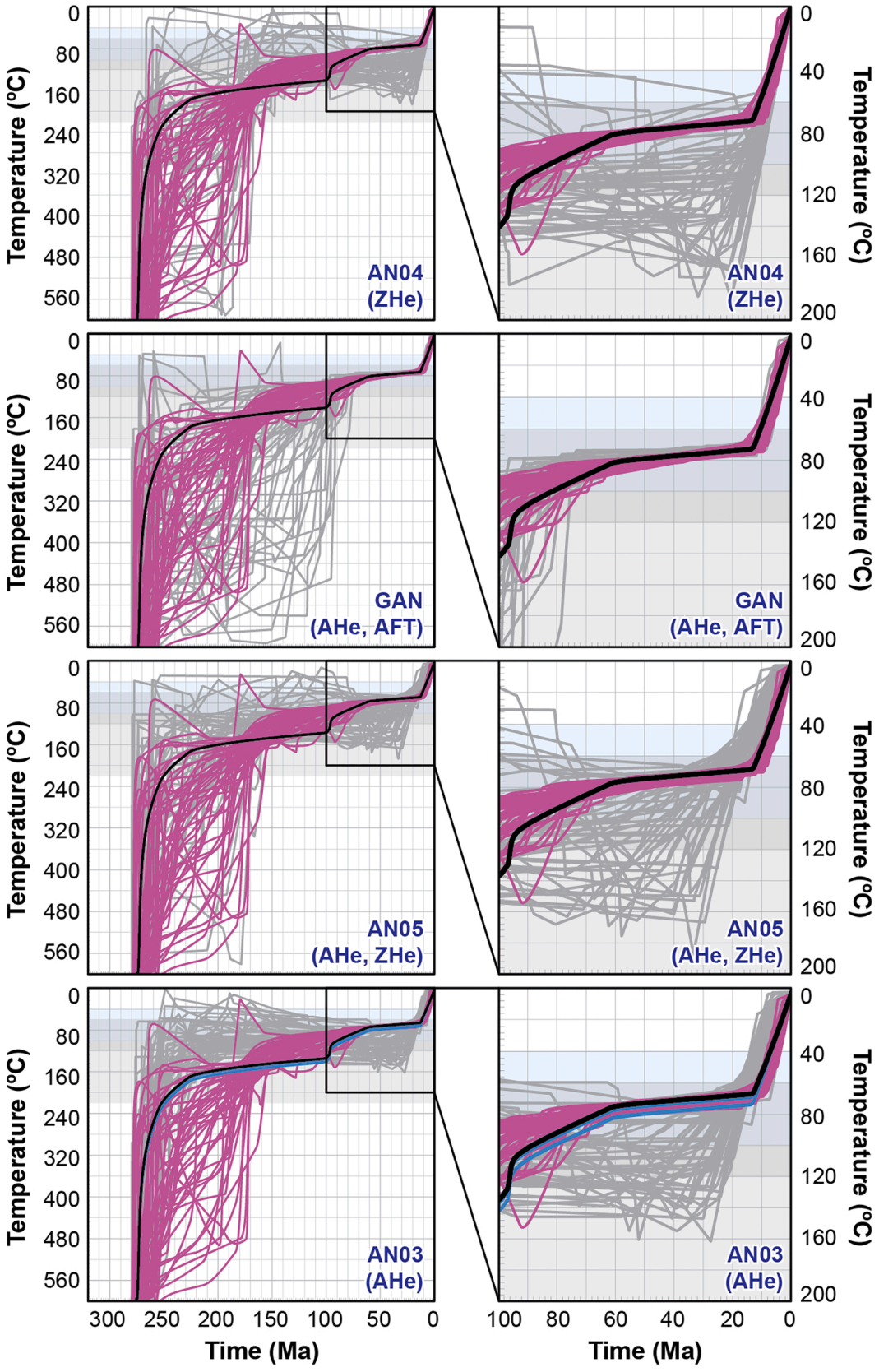

Fig. 7. Comparison of single- vs. multi-sample HeFTy inversion results for the Agua Negra pluton. Purple lines denote the 50 "good"-fit paths obtained by the multi-sample model; best-fit paths are shown in black or teal as in Fig. 6. Grey lines illustrate the 50 "good"-fit paths yielded by single-sample models using the same thermochronologic data (Tables 1, S6; Fig. S2). Horizontal blue and grey bars highlight nominal partial retention/annealing zones for the AHe, AFT, and ZHe systems (Gleadow et al., 1986; Ketcham et al., 2007; Flowers et al., 2009). Left column displays thermal histories from 320 to 0 Ma; right column shows time-temperature paths for the same samples at 0–100 Ma.

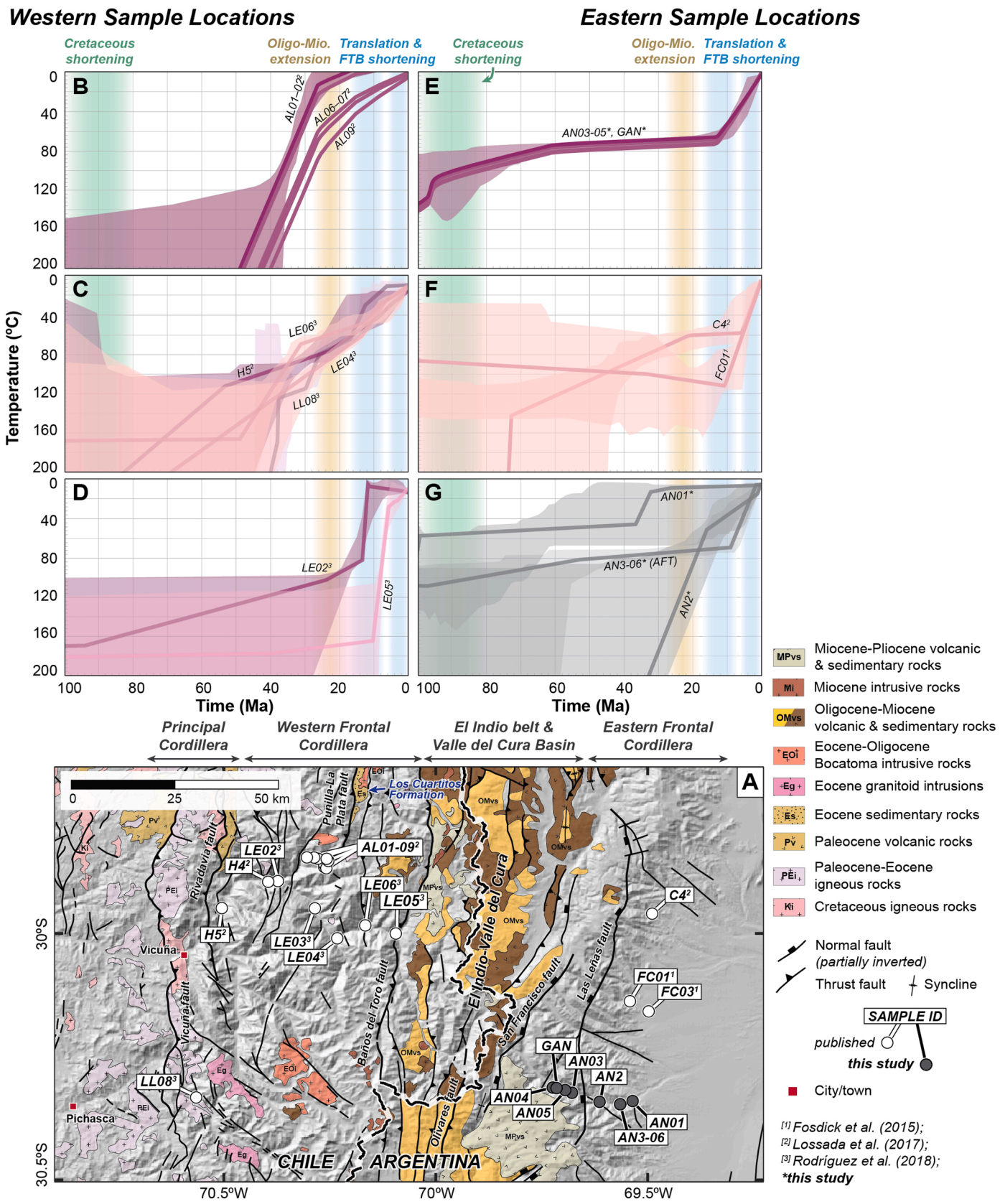

Fig. 8. (A) Hillshade map illustrating new and published thermochronology samples, major structures, and locations of Cretaceous and younger igneous rocks. (B-G) HeFTy inversion results for 100 to 0 Ma time interval. Best-fit paths shown in solid lines; transparent regions define envelopes of "good"-fit paths for each model. Color of "good"-fit envelopes and best-fit paths corresponds to color of sample symbols in Fig. 2. Detailed input information and individual models are presented in Tables 1, S6 and Figs. 5–6, S3, S5, and S13.

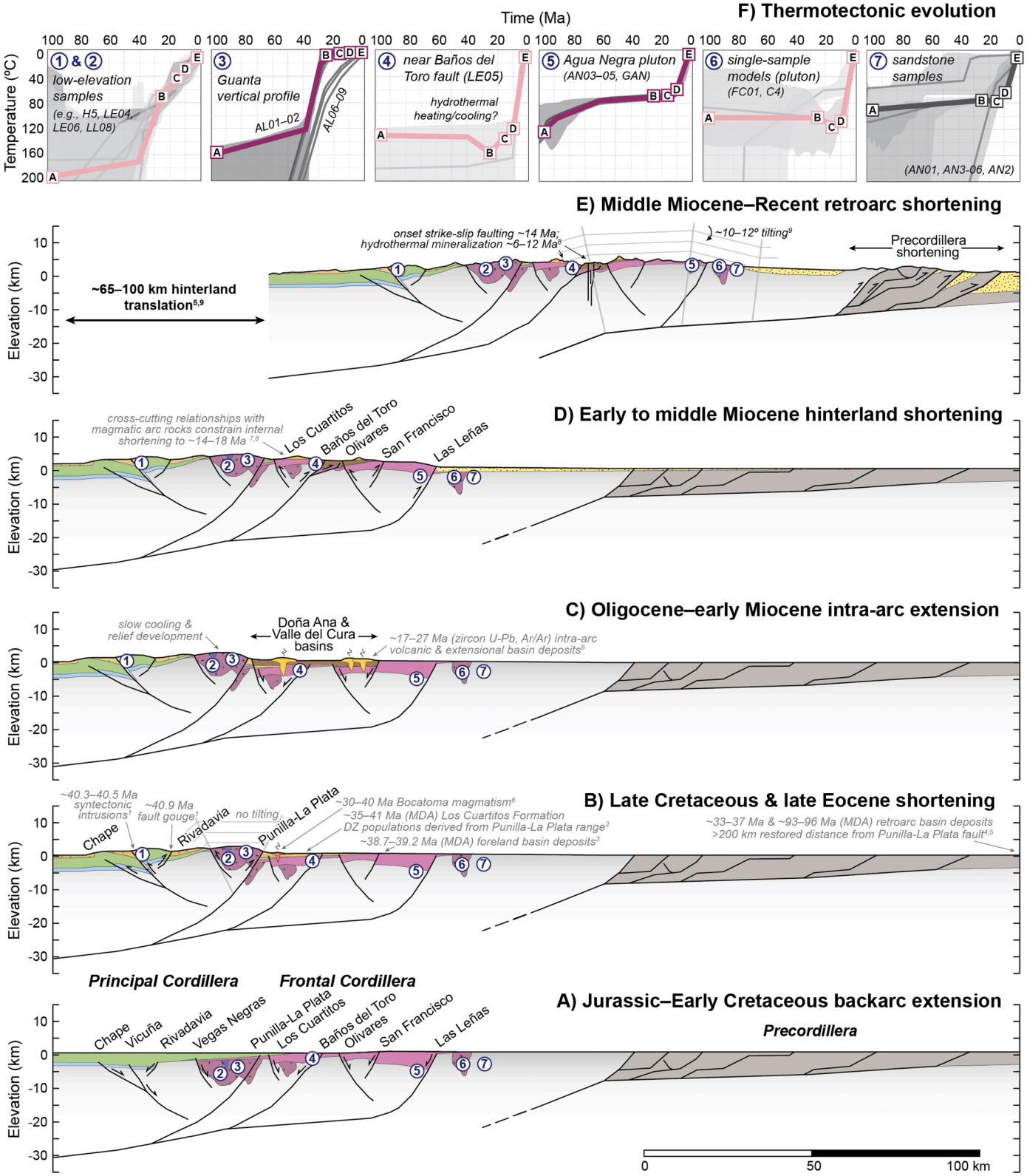

[1] Emparán & Pineda (1999); [2] Murillo et al. (2017); [3] Suriano et al. (2023); [4] Fosdick et al. (2017); [5] Mackaman-Lofland et al. (2022); [6] Litvak et al. (2018); [7] Bissig et al. (2001); [8] Giamgiagi et al. (2017); [9] Allmendinger et al. (1990); ***this study**

(caption on next page)

Fig. 9. Schematic cross-section reconstructions illustrating the Mesozoic-Cenozoic thermotectonic evolution of the Andean hinterland (Principal and Frontal Cordilleras) and external thrust belt (Precordillera) at ~30°S. Plots are arranged in chronological order, with the earliest reconstructions at the base. (A) Permian-Triassic and Jurassic-Early Cretaceous extension, thermal subsidence, and volcanic/volcaniclastic basin accumulation in the Principal Cordillera and western Frontal Cordillera. (B) Late Cretaceous and late Eocene shortening intervals, punctuated by Paleocene volcanism during neutral tectonic conditions. Grey lines illustrate schematic orientation and kink band information for the structures driving late Eocene exhumational cooling in the western Frontal Cordillera. (C) Oligocene-Early Miocene intra-arc extension and volcanic/volcaniclastic accumulation in the El Indio-Valle del Cura region. (D) Early-middle Miocene shortening and magmatism in the eastern (retroarc) hinterland and accumulation of lower foreland basin deposits. (E) Middle Miocene-Quaternary retroarc shortening in the Precordillera thrust belt, retroarc hinterland translation along the west-dipping regional décollement, and transition to strike-slip faulting and hydrothermal mineralization in the El Indio-Valle del Cura region. Grey lines illustrate schematic orientation and kink band information associated with hinterland fault-bend fold development kinematically linked to retroarc shortening. (F) "Good"-fit envelopes and best-fit paths from HeFTy inversions for 0–100 Ma time interval (as shown in Fig. 8; grey regions and thin grey lines), overlain with thermal history interpretations based on the schematic cross-sections and tectonothermal events illustrated in A-E. Numbered circles in A-E correspond to locations of thermochronology sample groups and model results shown in F.

kinematically linked to Precordillera structures and tilting of eastern Frontal Cordillera sample locations along the ~10–12° east-dipping forelimb of the resulting fault-bend fold (Fig. 9E).

The magnitude of hinterland translation and position of the footwall ramp are directly related to the amount of shortening accommodated in the Precordillera (estimates for which span ~65–100 km; Allmendinger and Judge, 2014; Mardonez et al., 2020). Structural, thermokinematic, and geomorphological studies further demonstrate the strong correspondence between regions of high topography and the position of major ramps in the décollement (Eizenhöfer et al., 2019). Our preferred interpretation thus places the ramp beneath the western flank of the zone of highest hinterland topography—the width and morphology of which align with the magnitude, duration, and rates of lateral advection required by Precordillera reconstructions (Figs. 2B, 9E). Our interpretation is further compatible with a pronounced ~14 Ma shift from shortening to strike-slip deformation in the El Indio-Valle del Cura region, possibly driven by an increase in the vertical (gravitational) stress component during compression and crustal thickening and accompanied by magma and hydrothermal fluid ascent along deeply rooted strike-slip faults (Giambiagi et al., 2017; Fig. 9E).

The transition to flat-slab subduction was accompanied by the inboard expansion then cessation of hinterland magmatism at ~9–6 Ma, concurrent with hydrothermal mineralization and the formation of major ore deposits in the El Indio-Valle del Cura region at ~12–6 Ma (Bissig et al., 2001; Ramos et al., 2002). Given this history and the ~14 Ma shift to a strike-slip-dominated hinterland stress regime, rapid ~10–8 Ma cooling documented for sample LE05 most likely reflects magmatic or hydrothermal heating/cooling associated with mineralization (Figs. 8D, 9E-F).

5.3. *Implications for the mechanisms driving hinterland construction*

Our five-step model reconstruction of thermotectonic events (Fig. 9) provides a framework in which to evaluate the processes driving construction of the Andean hinterland at ~30°S. Internal shortening was a chief driver of local exhumational cooling in the western Frontal Cordillera during the late Eocene, and crosscutting relationships indicate later internal shortening in the eastern Frontal Cordillera during the early to middle Miocene (Giambiagi et al., 2017; Murillo et al., 2017; Velásquez et al., 2021). However, internal shortening largely predates the main phase of Andean crustal thickening and flexural basin accumulation that signals development of a thick, elevated hinterland domain. Most crustal thickening, tectonic loading, and retroarc hinterland exhumation occurred after ~16–15 Ma, during high-magnitude shortening in the Precordillera thrust belt, retroarc hinterland translation along a regionally connected décollement, and a sharp decrease in the volume of arc magmatism (Allmendinger et al., 1990; Giambiagi et al., 2017; Litvak et al., 2018; Mackaman-Lofland et al., 2022; Suriano et al., 2017). Deeper processes such as lower crustal flow or lithospheric foundering are most robustly identified by rapid changes in crustal/lithospheric thickness or topography that are clearly decoupled—in terms of their timing, nature, and magnitude—from upper-crustal deformation events (e.g., Carrapa et al., 2022). At ~30°S, however, results of this study show that the timing and magnitude of hinterland crustal thickening, topographic growth, and Precordillera shortening are all tightly connected. These relationships point to westward underthrusting of cratonic lithosphere as the dominant mechanism controlling crustal thickening and topographic growth during hinterland construction (e.g., Long, 2023), most notably for the highest elevation retroarc hinterland domain (Figs. 2B, 9E).

6. Conclusions

New and published geochronology and low-temperature thermochronology (AHe, AFT, and ZHe) analyses, thermal history models, and structural, magmatic, and sedimentological datasets reveal two episodes of shortening-induced uplift and exhumational cooling during construction of the Andean hinterland at ~30°S. The first, at ~40–30 Ma, was characterized by ~120°C of rapid cooling (or ~3–6 km exhumation) during internal shortening and synorogenic sedimentation in the Principal and western Frontal Cordilleras. The second, at ~15–5 Ma, involved <60–120°C of rapid cooling (~2–4 km exhumation) along the eastern flank of the Frontal Cordillera and was synchronous with (1) the transition from hinterland shortening to strike-slip deformation in the El Indio-Valle del Cura region and (2) slow cooling, erosion, and topographic relief development west of the Punilla-La Plata fault. Results demonstrate the utility of multi-sample thermal history models in testing spatial, structural, and thermal hypotheses: models from the western hinterland require topographic relief development with no tilting of sample positions during exhumational cooling, while samples from the eastern (retroarc) hinterland point to both relief development and 10° east-down tilting during cooling. The spatiotemporal co-occurrence of hinterland thickening, exhumation/cooling, topographic growth, Precordillera shortening, and synorogenic sedimentation after ~16–15 Ma highlights westward underthrusting of cratonic lithosphere—rather than internal deformation, magmatic addition, lower crustal flow, or deeper processes associated with lithospheric foundering, mantle convection, or subduction dynamics—as the dominant mechanism controlling construction of the thick, elevated hinterland domain.

CRediT authorship contribution statement

Chelsea Mackaman-Lofland: Conceptualization, Data curation, Formal analysis, Funding acquisition, Investigation, Methodology, Visualization, Writing – original draft. **Ana C. Lossada:** Formal analysis, Investigation, Resources, Validation, Writing – review & editing. **Julie C. Fosdick:** Investigation, Methodology, Resources, Validation, Writing – review & editing. **Vanesa D. Litvak:** Investigation, Resources, Validation, Writing – review & editing. **María Pía Rodríguez:** Resources, Validation, Writing – review & editing. **Macarena Bertoa del Llano:** Investigation, Resources, Visualization, Writing – review & editing. **Richard A. Ketcham:** Methodology, Software, Validation, Writing – review & editing. **Daniel F. Stockli:** Resources. **Brian K. Horton:** Resources, Writing – review & editing. **José Mescua:** Resources, Writing – review & editing. **Julieta Suriano:** Resources, Writing – review &

editing. **Laura Giambiagi:** Resources, Writing – review & editing.

Declaration of competing interest

The authors declare that they have no known competing financial interests or personal relationships that could have appeared to influence the work reported in this paper.

Data availability

Data are available in the Supplemental Materials.

Acknowledgements

We thank Rebecca Vanderleest, Lucas Lothari, Erik Klemetti, and Sam Robbins for logistical aid, discussion, and assistance with data visualization. Des Patterson, Rudra Chatterjee, and Lisa Stockli provided valuable laboratory support. This research was supported by NSF grant 1952791 to CML, funding from projects PICT 2021-I-A-01210 and SIIP-UNCUYO M052-T1 to JFM, and by a grant from LA.TE. Andes S.A. and CONICET for analysis and processing samples from research projects. LA.TE. Andes S.A. is exclusively responsible for the quality of the data generated and not for the implications of its application. This is a N°R-488 contribution of the Instituto de Estudios Andinos Don Pablo Groeber (IDEAN, UBA-CONICET). We are grateful for constructive comments from Sean Long, two anonymous reviewers, and editorial support from Alex Webb.

Supplementary materials

Supplementary material associated with this article can be found online at doi:10.1016/j.epsl.2024.118888.

References

Allmendinger, R.W., Figueroa, D., Snyder, D., Beer, J., Mpodozis, C., Isacks, B.L., 1990. Foreland shortening and crustal balancing in the Andes at 30°S latitude. Tectonics. 9 (4), 789–809.
Allmendinger, R.W., Judge, P.A., 2014. The Argentine Precordillera: a foreland thrust belt proximal to the subducted plate. Geosphere 10 (6), 1203–1218.
Ammirati, J.B., Mackaman-Lofland, C., Zeckra, M., Gobron, K., 2022. Stress transmission along mid-crustal faults highlighted by the 2021 Mw 6.5 San Juan (Argentina) earthquake. Sci. Rep. 12 (1), 17939.
Beck, S.L., Zandt, G., 2002. The nature of orogenic crust in the Central Andes. J. Geophys. Res. 107, 2230.
Bissig, T., Lee, J.K., Clark, A.H., Heather, K.B., 2001. The Cenozoic history of volcanism and hydrothermal alteration in the central Andean flat-slab region: new 40Ar-39Ar constraints from the El Indio–Pascua Au (-Ag, Cu) belt, 29 20′–30 30′ S. Int. Geol. Rev. 43 (4), 312–340.
Capaldi, T.N., McKenzie, N.R., Horton, B.K., Mackaman-Lofland, C., Colleps, C.L., Stockli, D.F., 2021. Detrital zircon record of Phanerozoic magmatism in the southern Central Andes. Geosphere 17 (3), 876–897.
Cardó, R., Díaz, I.M., 2005. Hoja Geológica 3169-I Rodeo (Vol. 272, p. 52). Instituto de Geología y Recursos Minerales, Servicio Geológico Minero Argentino.
Carrapa, B., DeCelles, P.G., Ducea, M.N., Jepson, G., Osakwe, A., Balgord, E., Stevens Goddard, A.L., Giambiagi, L.A., 2022. Estimates of paleo-crustal thickness at Cerro Aconcagua (Southern Central Andes) from detrital proxy-records: implications for models of continental arc evolution. Earth Planet. Sci. Lett. 585, 117526.
Charrier, R., Pinto, L., & Rodríguez, M.P. (2007). Tectonostratigraphic evolution of the Andean Orogen in Chile.
Coutts, D.S., Matthews, W.A., Hubbard, S.M., 2019. Assessment of widely used methods to derive depositional ages from detrital zircon populations. Geoscience Frontiers 10 (4), 1421–1435.
Cristallini, E.O., Ramos, V.A., 2000. Thick-skinned and thin-skinned thrusting in the La Ramada fold and thrust belt: crustal evolution of the High Andes of San Juan, Argentina (32 SL). Tectonophysics. 317 (3–4), 205–235.
Dávila, F.M., Lithgow-Bertelloni, C., 2015. Dynamic uplift during slab flattening. Earth Planet. Sci. Lett. 425, 34–43.
Dickinson, W.R., Gehrels, G.E., 2009. Use of U–Pb ages of detrital zircons to infer maximum depositional ages of strata: a test against a Colorado Plateau Mesozoic database. Earth Planet. Sci. Lett. 288 (1–2), 115–125.
Eizenhöfer, P.R., McQuarrie, N., Shelef, E., Ehlers, T.A., 2019. Landscape response to lateral advection in convergent orogens over geologic time scales. Journal of Geophysical Research: Earth Surface 124 (8), 2056–2078.
Emparán, C., Pineda, G.F., 1999. Geología Del Area Condoriaco-Rivadavia, Región de Coquimbo. Servicio Nacional De Geología y Minería, 12. Serie Geología Básica, Carta Geológica de Chile. Scale: 1:100,000.
Flowers, R.M., Ketcham, R.A., Shuster, D.L., Farley, K.A., 2009. Apatite (U–Th)/He thermochronometry using a radiation damage accumulation and annealing model. Geochim. Cosmochim. Acta 73 (8), 2347–2365.
Flowers, R.M., Farley, K.A., Ketcham, R.A., 2015. A reporting protocol for thermochronologic modeling illustrated with data from the Grand Canyon. Earth Planet. Sci. Lett. 432, 425–435.
Flowers, R.M., Zeitler, P.K., Danišík, M., Reiners, P.W., Gautheron, C., Ketcham, R.A., Metcalf, J.R., Stockli, D.F., Enkelmann, E., Brown, R.W., 2023a. (U-Th)/He chronology: part 1. Data, uncertainty, and reporting. GSA Bulletin, 135 (1–2), 104–136.
Flowers, R.M., Ketcham, R.A., Enkelmann, E., Gautheron, C., Reiners, P.W., Metcalf, J.R., Danišík, M., Stockli, D.F., Brown, R.W., 2023b. U-Th)/He chronology: part 2. Considerations for evaluating, integrating, and interpreting conventional individual aliquot data. GSA Bulletin 135 (1–2), 137–161.
Fosdick, J.C., Carrapa, B., Ortíz, G., 2015. Faulting and erosion in the Argentine Precordillera during changes in subduction regime: reconciling bedrock cooling and detrital records. Earth Planet. Sci. Lett. 432, 73–83.
Fosdick, J.C., Reat, E.J., Carrapa, B., Ortiz, G., Alvarado, P.M., 2017. Retroarc basin reorganization and aridification during Paleogene uplift of the southern central Andes. Tectonics. 36 (3), 493–514.
Galbraith, R.F., 1981. On statistical models for fission track counts. Journal of the International Association for Mathematical Geology 13 (6), 471–478.
Giambiagi, L., Álvarez, P.P., Creixell, C., Mardonez, D., Murillo, I., Velásquez, R., Lossada, A.C., Suriano, J., Mescua, J., Barrionuevo, M., 2017. Cenozoic shift from compression to strike-slip stress regime in the high Andes at 30 S, during the shallowing of the slab: implications for the El Indio/Tambo mineral district. Tectonics. 36 (11), 2714–2735.
Giambiagi, L., Tassara, A., Echaurren, A., Julve, J., Quiroga, R., Barrionuevo, M., Liu, S., Echeverría, I., Mardónez, D., Suriano, J., Mescua, J., Lossada, A.C., Spagnotto, S., Bertoa, M., Lothari, L., 2022. Crustal anatomy and evolution of a subduction-related orogenic system: insights from the Southern Central Andes (22–35° S). Earth. Sci. Rev., 104138
Gleadow, A.J., Duddy, I.R., Green, P.F., Lovering, J.F., 1986. Confined fission track lengths in apatite: a diagnostic tool for thermal history analysis. Contributions to Mineralogy and Petrology 94, 405–415.
Gleadow, A.J.W., Fitzgerald, P.G., 1987. Uplift history and structure of the Transantarctic Mountains: new evidence from fission track dating of basement apatites in the Dry Valleys area, southern Victoria Land. Earth Planet. Sci. Lett. 82 (1–2), 1–14.
Green, P.F., 1981. A new look at statistics in fission track dating. Nucl. Tracks. Radiat. Meas. 5 (1–2), 77–86.
Green, P.F., Duddy, I.R., Laslett, G.M., Hegarty, K.A., Gleadow, A.J.W., Lovering, J.F., 1989. Thermal annealing of fission tracks in apatite 4. Quantitative modelling techniques and extension to geological timescales. Chemical Geology: Isotope Geoscience section 79 (2), 155–182.
Guenthner, W.R., Reiners, P.W., Ketcham, R.A., Nasdala, L., Giester, G., 2013. Helium diffusion in natural zircon: radiation damage, anisotropy, and the interpretation of zircon (U-Th)/He thermochronology. Am. J. Sci. 313 (3), 145–198.
Hayes, G.P., Moore, G.L., Portner, D.E., Hearne, M., Flamme, H., Furtney, M., Smoczyk, G.M., 2018. Slab2, a comprehensive subduction zone geometry model. Science (1979) 362 (6410), 58–61.
Heredia, N., Fernández, L.R., Gallastegui, G., Busquets, P., Colombo, F., 2002. Geological setting of the Argentine Frontal Cordillera in the flat-slab segment (30° 00′–31° 30′ S latitude). J. South. Am. Earth. Sci. 15 (1), 79–99.
Hoke, G.D., Garzione, C.N., Araneo, D.C., Latorre, C., Strecker, M.R., Williams, K.J., 2009. The stable isotope altimeter: do Quaternary pedogenic carbonates predict modern elevations? Geology. 37 (11), 1015–1018.
Horton, B.K., Capaldi, T.N., Mackaman-Lofland, C., Perez, N.D., Bush, M.A., Fuentes, F., Constenius, K.N., 2022. Broken foreland basins and the influence of subduction dynamics, tectonic inheritance, and mechanical triggers. Earth Science Reviews 234.
Jones, R.E., Kirstein, L.A., Kasemann, S.A., Litvak, V.D., Poma, S., Alonso, R.N., Hinton, R., 2016. The role of changing geodynamics in the progressive contamination of Late Cretaceous to Late Miocene arc magmas in the southern Central Andes. Lithos. 262, 169–191.
Jordan, T.E., Allmendinger, R.W., Damanti, J.F., Drake, R.E., 1993. Chronology of motion in a complete thrust belt: the Precordillera, 30-31°S, Andes Mountains. J. Geol. 101, 135–156.
Ketcham, R.A., 2005. Forward and inverse modeling of low-temperature thermochronometry data. Rev. Mineral. Geochem. 58 (1), 275–314.
Ketcham, R.A., 2024. Thermal history inversion from thermochronometric data and complementary information: new methods and recommended practices. Chem. Geol. 653, 122042.
Ketcham, R.A., Carter, A., Donelick, R.A., Barbarand, J., Hurford, A.J., 2007. Improved modeling of fission-track annealing in apatite. American Mineralogist 92 (5–6), 799–810.
Ketcham, R.A., Gautheron, C., Tassan-Got, L., 2011. Accounting for long alpha-particle stopping distances in (U–Th–Sm)/He geochronology: refinement of the baseline case. Geochim. Cosmochim. Acta 75 (24), 7779–7791.
Ketcham, R.A., Mora, A., Parra, M., 2018. Deciphering exhumation and burial history with multi-sample down-well thermochronometric inverse modelling. Basin Research 30, 48–64.

Kleiman, L.E., Japas, M.S., 2009. The Choiyoi volcanic province at 34° S–36° S (San Rafael, Mendoza, Argentina): implications for the Late Palaeozoic evolution of the southwestern margin of Gondwana. Tectonophysics. 473 (3–4), 283–299.
Levina, M., Horton, B.K., Fuentes, F., Stockli, D.F., 2014. Cenozoic sedimentation and exhumation of the foreland basin system preserved in the Precordillera thrust belt (31–32°S), southern central Andes. Argentina. Tectonics 33, 1659–1680.
Litvak, V.D., Poma, S., Kay, S.M., 2007. Paleogene and Neogene magmatism in the Valle del Cura region: new perspective on the evolution of the Pampean flat slab, San Juan province, Argentina. J. South. Am. Earth. Sci. 24 (2–4), 117–137.
Litvak, V.D., Poma, S., Jones, R.E., Fernández Paz, L., Iannelli, S.B., Spagnuolo, M., Kirstein, L.A., Folguera, A., Ramos, V.A, 2018. The late Paleogene to Neogene volcanic arc in the southern Central Andes (28–37 S). The Evolution of the Chilean-Argentinean Andes 503–536.
Long, S.P., 2023. Westward underthrusting of thick North American crust: the dominant thickening process that built the Cordilleran orogenic plateau. Geology. 51 (12), 1111–1116.
Lossada, A.C., Giambiagi, L., Hoke, G.D., Fitzgerald, P.G., Creixell, C., Murillo, I., Mardonez, D., Velásquez, R., Suriano, J., 2017. Thermochronologic evidence for late Eocene Andean mountain building at 30 S. Tectonics. 36 (11), 2693–2713.
Ludwig, K.R., 2008. Isoplot 3.7 (Vol. 4, p. 77). Berkeley Geochronology Center Special Publication.
Ludwig, K.R., Mundil, R., 2002. Extracting reliable U-Pb ages and errors from complex populations of zircons from Phanerozoic tuffs. Geochim. Cosmochim. Acta 66. A463–463.
Mackaman-Lofland, C., Horton, B.K., Fuentes, F., Constenius, K.N., Stockli, D.F., 2019. Mesozoic to Cenozoic retroarc basin evolution during changes in tectonic regime, southern Central Andes (31–33 S): insights from zircon U-Pb geochronology. J. South. Am. Earth. Sci. 89, 299–318.
Mackaman-Lofland, C., Horton, B.K., Ketcham, R.A., McQuarrie, N., Fosdick, J.C., Fuentes, F., Constenius, K.N., Capaldi, T.N., Stockli, D., Alvarado, P., 2022. Causes of variable shortening and tectonic subsidence during changes in subduction: insights from flexural thermokinematic modeling of the Neogene southern central Andes (28–30 S). Tectonics. 41 (8) e2022TC007334.
Mardonez, D., Suriano, J., Giambiagi, L., Mescua, J., Lossada, A., Creixell, C., Murillo, I., 2020. The Jáchal river cross-section revisited (Andes of Argentina, 30 S): constraints from the chronology and geometry of Neogene synorogenic deposits. J. South. Am. Earth. Sci. 104, 102838.
McQuarrie, N., 2002. The kinematic history of the central Andean fold-thrust belt, Bolivia: implications for building a high plateau. Geol. Soc. Am. Bull. 114 (8), 950–963.
Mpodozis, C., & Ramos, V. (1990). The Andes of Chile and Argentina.
Murillo, I.R., Velásquez, R.H., Creixell, C.T., 2017. Geología de las áreas Guanta–Los Cuartitos y Paso de Vacas Heladas, regiones de Atacama y Coquimbo. Servicio Nacional de Geología y Minería. Carta Geológica de Chile. Serie Geología Básica 192–193. Scale: 1:100,000.
Murray, K.E., Braun, J., Reiners, P.W., 2018. Toward robust interpretation of low-temperature thermochronometers in magmatic terranes. Geochemistry, Geophysics, Geosystems 19 (10), 3739–3763.
Ramos, V.A., Cristallini, E.O., Pérez, D.J., 2002. The Pampean flat-slab of the Central Andes. J. South. Am. Earth. Sci. 15 (1), 59–78.
Ramos, V.A., Folguera, A., 2009. Andean Flat-Slab Subduction Through Time, 327. Geological Society, London, pp. 31–54. Special Publications.
Reiners, P.W., Farley, K.A., 2001. Influence of crystal size on apatite (U–Th)/He thermochronology: an example from the Bighorn Mountains. Wyoming. Earth and Planetary Science Letters 188 (3–4), 413–420.
Reiners, P.W., Brandon, M.T., 2006. Using thermochronology to understand orogenic erosion. Annu. Rev. Earth Planet. Sci. 34, 419–466.
Rodríguez, M.P., Charrier, R., Brichau, S., Carretier, S., Farías, M., de Parseval, P., Ketcham, R.A., 2018. Latitudinal and longitudinal patterns of exhumation in the Andes of north-central Chile. Tectonics. 37 (9), 2863–2886.
Sato, A.M., Llambías, E.J., Basei, M.A., Castro, C.E., 2015. Three stages in the Late Paleozoic to Triassic magmatism of southwestern Gondwana, and the relationships with the volcanogenic events in coeval basins. J. South. Am. Earth. Sci. 63, 48–69.
Suriano, J., Mardonez, D., Mahoney, J.B., Mescua, J.F., Giambiagi, L., Kimbrough, D., Lossada, A., 2017. Uplift sequence of the Andes at 30°S: insights from sedimentology and U/Pb dating of synorogenic deposits. J. South. Am. Earth. Sci. 75, 11–34.
Suriano, J., Lossada, A.C., Mahoney, J.B., Tedesco, A.M., Limarino, C.O., Giambiagi, L.B., Mazzitelli, M.A., Mescua, J.F., Lothari, L., & Quiroga, R. (2023). The Southern Extension of the Eocene Andean orogeny: New sedimentary Record of the Foreland Basin in the Southern Central Andes At 32°S. Basin Research.
Val, P., Hoke, G.D., Fosdick, J.C., Wittmann, H., 2016. Reconciling tectonic shortening, sedimentation and spatial patterns of erosion from 10Be paleo-erosion rates in the Argentine Precordillera. Earth Planet. Sci. Lett. 450, 173–185.
Velásquez, R.H., Coloma, F.B., Murillo, I.R., Merino, R.G., Ortiz, M.L., 2021. Geología de las áreas Pisco Elqui y Paso del Agua Negra, región de Coquimbo. Servicio Nacional de Geología y Minería. Carta Geológica de Chile. Serie Geología Básica 211–212. Scale: 1:100,000.
Winocur, D.A., Litvak, V.D., Ramos, V.A., 2015. Magmatic and tectonic evolution of the Oligocene Valle del Cura basin, main Andes of Argentina and Chile: evidence for generalized extension. Geological Society 399 (1), 109–130. Special Publications.
Yáñez, G.A., Ranero, C.R., von Huene, R., Díaz, J., 2001. Magnetic anomaly interpretation across the southern central Andes (32–34 S): the role of the Juan Fernández Ridge in the late Tertiary evolution of the margin. J. Geophys. Res.: Solid Earth 106 (B4), 6325–6345.